Chemical Engineering Journal 488 (2024) 150856

Contents lists available at ScienceDirect

Chemical Engineering Journal

journal homepage: www.elsevier.com/locate/cej

Supercritical water oxidation using hydrothermal flames at microscale as a potential solution for organic waste treatment in space applications – A practical demonstration and numerical study

Deewakar Sharma [a], Olivier Nguyen [a], Fabien Palencia [a], Carole Lecoutre [a], Yves Garrabos [a], Stéphane Glockner [b], Samuel Marre [a,*], Arnaud Erriguible [a,b,*]

[a] Univ. Bordeaux, CNRS, Bordeaux INP, ICMCB, UMR5026, F-33600, Pessac, France
[b] Univ. Bordeaux, CNRS, Bordeaux INP, I2M, UMR5295, F-33600, Pessac, France

ARTICLE INFO

Keywords:
High pressure microfluidics
Supercritical water oxidation
Hydrothermal flames
Simulation
Life support system for space applications

ABSTRACT

Supercritical water oxidation (SCWO) with hydrothermal flames is well established for the treatment of aqueous organic waste as it not only overcomes the limitations of simple SCWO, such as precipitation of salts, but also exhibits many advantages over other waste treatment processes. Seeking these advantages, we propose to perform SCWO using hydrothermal flames in microfluidic reactors ($\mu SCWO$) for aerospace applications to be used in deep space/ISS missions. The novelty and highlight of this work are successful demonstration of realizing microreactors (channel width 200 μm), which can withstand pressure of 250 bar with temperature 400 °C, thereby presenting the feasibility to realize this technology. We present the first evidence of SCWO/hydrothermal in a flow microreactor of sapphire, which is captured through optical visualization. This is followed by a numerical investigation to understand the underlying physics leading to the formation of hydrothermal flame and thus differentiate it from a simple SCWO reaction. The simulations are performed in a 2D domain in a co-flow configuration with equal inlet velocity of fuel and oxidizer at two different inlet temperatures (350 °C and 365 °C), just below the critical temperature of water using ethanol and oxygen, the former acting not only as a model organic matter but also fuel for the formation of hydrothermal flames. It is observed that due to microscale size of the system, hydrothermal flames are formed at low inlet velocities (< 30 mm/s), while reaction at higher ones are characterized as simple SCWO reaction. This upper limit of inlet velocity was found to increase with inlet temperature. Finally, some key characteristics of hydrothermal flames - ignition delay time, flame structure, shape, and local propagation speed are analyzed.

1. Introduction

The need for organic wastes treatment has led to the development of several prominent solutions, most of them being oxidation-based destruction methods, namely activated carbon treatment, biological treatment, wet air oxidation, and supercritical water oxidation (SCWO) [1,2]. Among these, SCWO has gained significant attention in recent years owing to its several advantages over its counterparts, such as homogenous medium for oxidation, absence of NO_x formation and the ability to be energy-efficient in a certain range of organic wastes concentration in aqueous media (5—40 wt%) compared to other processes. The products obtained are primarily water and carbon dioxide (CO_2). The characteristics of SCWO arise from the peculiar thermophysical properties of water above its critical point ($T = 374^{\circ}C, P = 22.1MPa$). Of particular relevance to SCWO are the significant reduction of the dielectric constant and ionic product of water at its supercritical conditions. The former causes a change in the polarity of the water rendering supercritical water (SCW) non-polar in nature. Consequently, it acts as a very good solvent for the organic matter as well as several nonpolar gases such as, oxygen, nitrogen etc., making it a homogenous medium for the oxidation of the former. This not only circumvents the limitations posed by interfacial mass transfer, but also facilitates very fast reaction and high destruction efficiencies close to unity (up to 99.9 %) [1,2]. Likewise, the low ionic product results in the dominance of free radical mechanisms in SCW resulting in high solubility of organic matter [3,4]. Despite these advantages, the SCWO process faced two

* Corresponding authors at: Univ. Bordeaux, CNRS, Bordeaux INP, ICMCB, UMR5026, F-33600, Pessac, France (S. Marre and A. Erriguible).
E-mail addresses: Samuel.marre@icmcb.cnrs.fr (S. Marre), erriguible@enscbp.fr (A. Erriguible).

https://doi.org/10.1016/j.cej.2024.150856
Received 23 December 2023; Received in revised form 4 March 2024; Accepted 30 March 2024
Available online 31 March 2024

major challenges [2,5]. Firstly, corrosion of the process equipment due to reactive ions such as Cl^-, F^- and secondly, plugging of the reactors/ process equipment due to the precipitation of inorganic salts. A well-sought approach to address these limitations consists in injecting the reactants (water, organic waste, etc.) at sub-critical conditions ($T < T_c$) and attaining supercritical conditions, primarily in terms of temperature, inside the reactor. This is made possible by utilizing the heat generated by hydrothermal flames - the flames which ignite in supercritical water. These were initially observed by Schilling and Franck, [6] while carrying out supercritical water oxidation of highly concentrated methane. In addition to addressing the aforementioned limitations, using hydrothermal flames further enhance the SCWO process capabilities, namely, higher temperature during the reaction resulting in nearly complete conversion of organic matter, further reduction in reaction time (reactions completing in few milliseconds), and reduction in the reactor size enabling high energy recovery. The generation of these flames is ascribed to the reduction of the auto-ignition temperature of organic matter (fuel) in SCW conditions. While some organic matter may be able to generate sufficient heat to autoignite, such as quinoline [7], in situations wherein organic water or wastewater may have a low heating value, a small amount of auxiliary fuel (usually methanol or isopropanol) is added to achieve auto thermal operation. In situations wherein organic water or wastewater may have a low heating value, a small amount of auxiliary fuel (usually methanol or isopropanol) is added to achieve auto thermal operation [8,9]. It is to be mentioned that the organic matter and oxygen present in the homogeneous medium (water) are always reacting and thus, heat is being consistently generated. However, it is only beyond a threshold - primarily in terms of concentration of the fuel and oxidizer at a given temperature and pressure - that the autoignition criteria is met and hydrothermal flames are formed. Thus, despite the reaction between organic matter and oxidizer being omnipresent in SCW conditions, the same cannot be asserted for the formation of hydrothermal flames.

Intrigued by this unique counter-intuitive phenomenon of having flames or *fire* in water, a significant amount of work has been done, both from experimental and numerical perspectives, to seek better understanding of this process. Some of the initial pioneering works were reported by ETH Zurich group [5,10–15] and High-Pressure Process (HPP) Group, Valladolid, Spain [8,16–19]. The research activities of ETH research group focused on utilizing hydrothermal flames for the treatment of organic pollutants [10,12,20] and hydrothermal spallation drilling [15,21–23]. Both the research groups have mainly used transpiring wall reactors for the treatment of wastewater and sludge in order to address the challenges of corrosion and salt deposition. In recent years, several other research groups have also successfully demonstrated different reactors to study hydrothermal flames. Sobhy *et al.* [24] designed a visual flame cell to observe the formation of hydrothermal flames, which was subsequently used to study the decomposition of naphthalene [25]. The authors observed up to 99.9 % destruction of naphthalene when the injected air temperature was increased to $400^{\circ}C$. Serikawa *et al.* [26] studied hydrothermal flames in a pilot scale reactor of 4800 *ml* in down flowing configuration using 2-propanol as the fuel. The authors drew a criterion of using fuel concentration higher than 2 vol % along with reactor temperature $> 470^{\circ}C$ for the generation of flames. Ren *et al.* [27] analyzed the characteristics of hydrothermal flames with a simple flow model using a detailed chemical kinetics for methanol oxidation. In their subsequent works [28], the authors studied extinction limits of non-premixed methanol hydrothermal flames using two different turbulent combustion models, namely Eddy dissipation concept (EDC) model and flamelet generated manifolds (FGM). A comprehensive review of different reactors along with their objectives is presented in the recent article by Cui *et al.* [29]. Off late, the utility of hydrothermal flames has also been investigated for power generation [30–32].

Exploring further avenues in utilizing hydrothermal flames, Hicks *et al.* [33] proposed to exploit the potential of hydrothermal flames for the treatment of organic/human waste for space applications. The motivation for using SCWO in space technology can be attributed to a recent increase in space activities envisioning deep space missions involving humans, which has created the need to develop technologies capable of sustaining life aboard these missions. The treatment of human/organic wastes and further conversion / valorization into useful products is one of the essential needs. In their initial works, the authors reported an ignition map for *n*-propanol as a model fuel in SCW [33] along with optimum reactor temperature for minimizing the ignition delay. More recently, the authors have studied hydrothermal flames using ethanol as fuel in co-flow configuration [34]. The incipient flames formed were found to propagate upstream, which subsequently resulted in a stable flame near the burner. Furthermore, flame emissions using spectroscopic measurements were analyzed over a wide range of wavelengths and emission band in the range of 350 *nm* to 540 *nm* was reported. The authors explained this observation due to the presence of carbon-dioxide radical (CO_2*).

While the work in [4,33,34] is commendable for advancing SCWO using hydrothermal flames for space applications, the size of the reactor considered is nearly the same order as those for ground-based applications ($O(l)$). It is intuitively quite challenging, if not unfeasible, to have a straightforward adaptation of a ground-based technological setup for space applications. One of the prime limitations arise from the size of the reactor and the overall system. In order to meet this constraint, there arises a need to miniaturize the SCWO process towards microscale. This would further bring in the advantages of microfluidics such as more uniformity in reactions, lower reaction times, etc. We define this novel approach as micro SCWO ($\mu SCWO$) / $\mu SCWO-H$, the latter being in the presence of hydrothermal flames. The feasibility to realize such a microreactor withstanding such extreme pressure and temperature conditions has already been demonstrated in [35], which was made possible through the development of a new patented a technology to fabricate microreactors out of sapphire [36]. Thanks to this new technology, we have design a specific test reactor on a chip able to implement SCWO process.

To further advance this technology, it is thereby essential to develop a fundamental understanding of the behavior of SCWO/hydrothermal flames at microscale. It is worth highlighting that the rich pertinent literature on SCWO and hydrothermal flames falls short to address the behavior in $\mu SCWO-H$ due to the following differences:

- (i) First, the large surface area to volume ratio at microscale, which results in higher heat loss and thus can result in different ignition conditions and flame characteristics.
- (ii) Second, unlike the ground-based applications where the temperature of the fuel and oxidizer stream entering the reactor could be ascertained to be same as that at the inlet and thus rendering more manual controllability, the microfluidic path to be traversed by the two streams will augment the fluid temperature close to that of microchip reactor temperature (due to rapid heat gain by the fluid at microscale). Thus, there is less control over individual stream temperatures before these enter the reactor channel.
- (iii) Lastly, the range of flow rates encountered at microscale is primarily laminar in nature and thus different from most of the existing meso/mini scale reactors for ground-based applications where a turbulent regime is generally encountered.

In quest of developing the proposed $\mu SCWO-H$ technology, we present in this work the feasibility to carry out $\mu SCWO$ in a flow process using hydrothermal flames at microscale. The first step illustrates that $\mu SCWO$/ $\mu SCWO-H$ reaction can be captured experimentally in a microreactor. The preliminary experimental observations have motivated further investigation of the $\mu SCWO-H$ to seek insights into the underlying physics, which was undertaken in the second step using numerical simulations. The modeling methodology is opted for saving

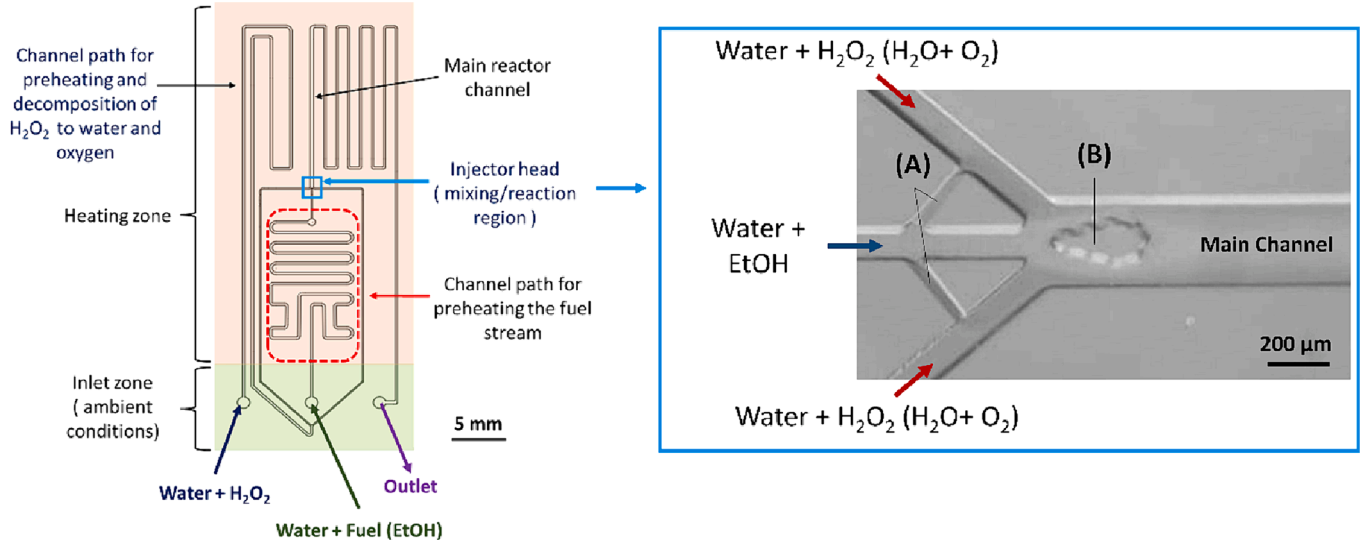

Fig. 1. (a) Schematic of the microreactor system proposed to be used for *µSCWO −H*.(b) Microscopy image of the injector head microfabricated in sapphire [35,37].

experimental time, while overcoming the complicated experimental characterization of the system, which poses severe limitations and challenges to gain understandings into behavior of the physical process at the local level. In this paper, we start by introducing the microreactor and the set-up design to carry out experimentally the *µSCWO* process. Then, we detail the visual observations obtained from *µSCWO/ µSCWO −H* during preliminary experiments. Thereby, we present the mathematical model used in the present work for the numerical process simulation, followed by its validation. Subsequently, results of the current problem are discussed, primarily - identify regimes corresponding to the hydrothermal flames as opposed to a simple SCWO reaction at microscale and developed understanding of the factors leading to the observed behavior. Characteristics of hydrothermal flames, such as ignition delay time, flame structure, at microscale are analyzed followed by perspectives for future work.

2. Experimental demonstration of the SCWO reaction in a sapphire microreactor - towards hydrothermal flames at microscale

2.1. Microreactor design

The overall scheme of the microreactor is shown in Fig. 1. The microreactor design is split into two sections: one section corresponding to the “injection zone”, where the temperature is maintained below 100 °C (ambient conditions) and the second section corresponding to the “reaction zone”, which is heated up to the operating temperature (300 < T(°C) ⟨500). Two separated inlets allow for the injection of both, the oxidizer stream (solution of H_2O_2 in water, 30 wt%) and the fuel stream (Ethanol /water, 30/ 70 %V/V). The two separated flows enter the microreactor and are brought to the desired working temperature thanks to pre-heating microchannels (serpentine networks, Fig. 1(a)). Both flowrates are controlled separately in the range 1 to 100 µL.min^{-1},

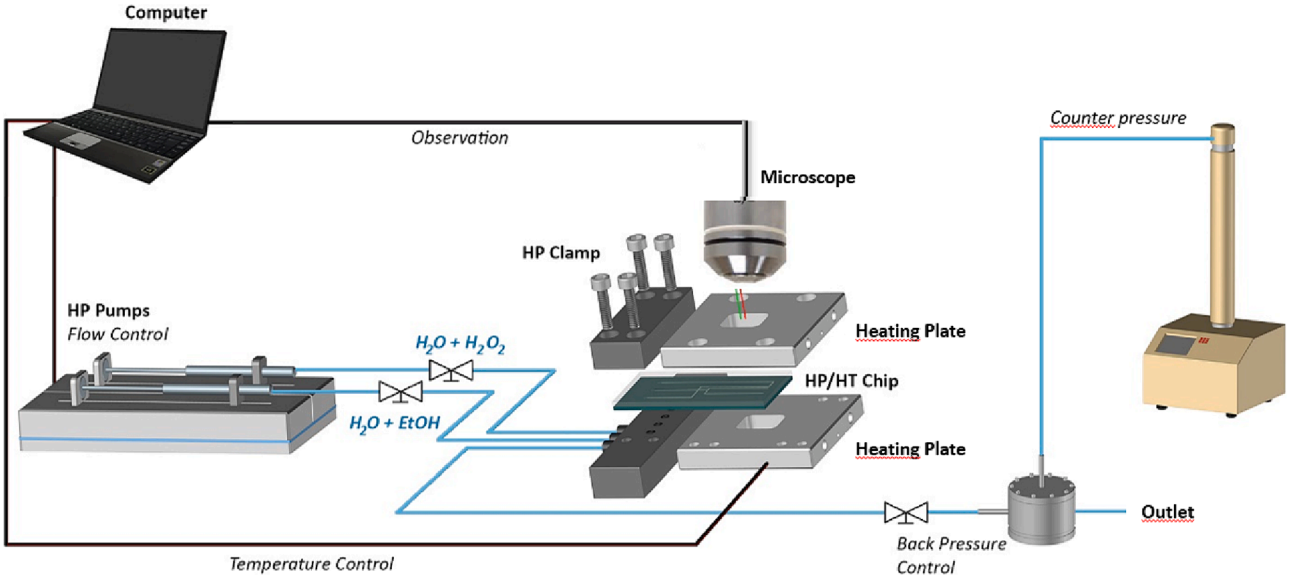

Fig. 2. *Schematic of the µSCWO −H set-up.*

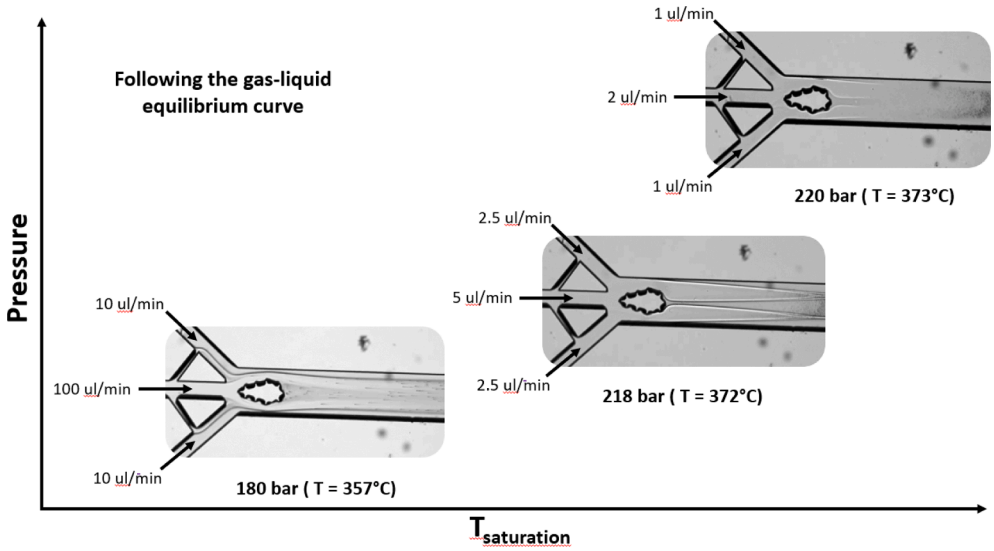

Fig. 3. *Observation of two-phase regimes at different pressures for a fixed heater temperature of 470°C.*

depending on the considered operating regimes and conditions. These microchannels have dimensions of 150μm in width and 40μm in depth, with a total flow length of $\approx$ 6cm for the fuel flow and $\approx$ 8cm for the oxidant flow. This configuration allows for a total decomposition of the hydrogen peroxide into water and O_2 before the mixing point. The oxidant flow is then split equally into two separated flows (microchannels width $=$ 150μm) before coming in contact with the oxidant stream in the "injector head" (Fig. 1(b)). In this design, the fuel stream is sandwiched between two oxidant flows, generating a 2D co-flow system. The reaction then occurs in the main reactor channel, which is 300 μm wide, 40 μm deep. While overall length of microreactor in the present work is 10cm(10,0000μm), the zone of interest is few *microns*(2500μm) which has been also considered in the simulations. In addition, the following design features were implemented for the experimental demonstration based on phenomenological understanding of the process. The side channel for secondary flow (Fig. 1(b) – A) were incorporated to ensure a pre-mixing zone of the reactants before they meet at injector head. Besides, an island was created just after the injector (Fig. 1 (b) – B) to ensure a better anchoring of the flame and avoid flame lifting during operation.

2.2. Experimental set-up

The schematic of the experimental set up is shown in Fig. 2. The microreactor is connected to the external fluidic system with the use of compression HP clamp, which was already reported elsewhere [38] and sandwiched between two aluminum heating plates containing heating cartridges. A thermocouple is placed alongside, connected to a ©Eurotherm system allowing generating the power required to controlled the temperature of the microreactor (±1K). Since we may have heat loss due to natural convection, the temperature of the microreactor can slightly differ from the input maintained at the heater. Thus, in order to have an estimate of the microreactor temperature, a thermocouple is also placed in contact with the surface of the microreactor. The microreactor is fed with two liquid streams using two high-pressure syringe pumps (©CETONI Nemesys HP pump), while the pressure in the system is maintained thanks to a membrane back-pressure regulator (©Equilibar, model: U6L), which pressure is controlled with the use of a ©Teledyne ISCO pump (model 100 DM) operated in constant pressure mode. The latter serves to maintain the outlet pressure, which was set between 150 and 250 bar, depending on the experiment. In order to visualize the flow dynamics, a small opening is made inside the heating plates and an optical microscope (©LEICA, model DM 2700) is placed over that window. As the sapphire microreactor is fully transparent, the observations are performed in transmission mode.

2.3. Preliminary experimental observations

In order to obtain hydrothermal flames at microscale, it is essential to ensure that the temperature of the fluids entering the microreactor is in close proximity to the critical temperature of the water (*i.e.,* 350 °C or higher). The fluids injected from the syringe pumps to the microreactor are at room temperature (20 °C – 25 °C) and they alleviate to the desired temperature inside the reactor thanks to the pre-heating microchannels. The flow paths of the two streams, as shown in schematic design of the microreactor in Fig. 1(a), is devised to facilitate this heating up. However, unlike other mini/meso scale SCWO systems, where the inlet temperature can be controlled and is thus known *a priori*, the current system makes it challenging to estimate the same. As attainment of appropriate temperature conditions inside the reactor forms a bottleneck of this whole process, a means to have an approximate estimate, if not precise, is essential to proceed further. An implicit approach was followed for this objective. The temperature at the surface of the microreactor could provide an estimate, or rather an upper limit of the temperature of the fluid entering the main reactor channel. This is because the temperature of the fluids will depend on their residence times inside the preheating channels (time taken for effective heat transfers from the surfaces to the fluids), which depends on the flowrates. Thus, the actual temperature could vary anywhere from room temperature (though least possible scenario) to the temperature at the reactor surface. In order to achieve the aforesaid objective, experiments were initially conducted using water injected from both inlets. The sought methodology is to have an estimate of the flow rate for a given heating plate temperature and microreactor surface temperature at which we could observe phase change behavior at a fixed pressure. Such an observation implies that the temperature of the water in the vapor phase entering the reactor channel is above the saturated temperature at the set pressure. This provides an estimate of the heater temperature required to raise the water temperature at least to the saturated temperature value. The significance of word at least can be justified as the vapor phase may not be necessarily at equilibrium conditions but may exist as superheated steam. Fig. 3 shows these observations at different pressures and flowrates marked in the figure itself. The temperature at the input heater was kept fixed at 470°C in the current case and saturated temperature for different pressures is also marked therein.

We observe a clear distinction between the two streams which can be

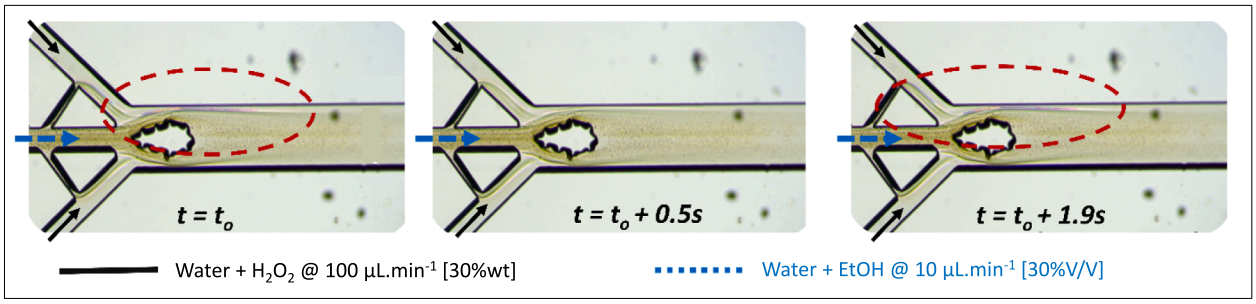

Fig. 4. *Appearance of blue regions in zone of interaction between fuel (ethanol) and oxidizer (oxygen) stream. The time instance when these are observed is arbitrarily defined as t_o.* (For interpretation of the references to color in this figure legend, the reader is referred to the web version of this article.)

regarded as an interface between the two phases - liquid water and water vapor. The observation can be ascribed to the fact that a lower flowrate entails a higher residence time of the fluid thereby resulting in longer heating time and subsequent phase change of water from liquid to vapor phase. Conversely, in case of a high flowrate, the water still remains in the liquid state. It can be inferred that for flowrates at which we observe a phase change, the temperature has exceeded the saturation temperature for that set pressure. It is worth mentioning that the operating pressure for SCWO being above the critical pressure of water, phase change cannot be observed and thus the temperature at 220 bar provides an estimate of the minimum temperature that needs to be set to ensure that water entering the reactor is close to its critical point. From the above observations, the temperature at the heater was set to 490$^{\circ}C$ for real SCWO experiments, which resulted in microreactor surface temperature to be 420$^{\circ}C$ for flowrates of 100 µL/min and 10 µL/min for the oxidant and fuel flows, respectively. In such conditions, we expect the temperature of the water to be in the range 350 −370$^{\circ}C$. It is to be mentioned that previous studies have shown the formation of hydrothermal flames even at subcritical conditions [22], which is also desired in the present context from process energy perspectives. Thus, the aforementioned conditions were considered optimal for the investigation of the *µSCWO* phenomenon.

The formation of hydrothermal flames is ascribed to the autoignition of organic matter (ethanol in the present case, which also acts as a fuel) in supercritical water in the presence of oxygen. The formation of products (and thus SCWO/hydrothermal flames) in the current setup can be identified by the appearance of blue regions – color of ethanol flame, primarily due to excited state of carbon dioxide. Fig. 4 shows the results obtained at flowrates of 100 µL.min^{-1} for the oxidant and 10 µL.min^{-1} for the fuel at P = 250 bar and $T_{surface}$ = 420 °C (*i.e.* estimated fluid temperature of 360 °C), as detailed previously. As mentioned, the purpose of presenting the experimental results is primarily demonstrating the feasibility to have SCWO/hydrothermal flames at microscale and thus, only the most relevant observations are illustrated. Here, t_0 refers to an arbitrary reference time. It can be seen that there exist blue regions where the fuel and oxidizer come in contact with each other, *i.e.* in the pre-mixing and the injector areas. These blue regions are intermittent in nature as they disappear after a small time and reappear again (t_0 +0.5*s* and t_0 + 1.9*s*, respectively). The following inferences are drawn from these observations. As the blue regions are formed where the fuel and oxidizer stream come in contact with each other, it arises due to interaction between the two streams *i.e.* reaction between ethanol and oxygen. With reaction being omnipresent in these conditions, the products, among which carbon dioxide is one of them, will always be formed. However, the intermittent nature of the blue color suggests that this particular observation represents the ignition kernel due to autoignition of ethanol and resulting in the formation of excited carbon dioxide (Fig. 4). The intermittent nature further indicates that the ignition kernel is not able to sustain the flame under the set conditions. This also highlights that even though reaction is always occurring, hydrothermal flames are feasible only for certain conditions governed by the coupled thermo-hydro-chemical dynamics. This thereby brings to an important question - what is the impact of flow conditions on *µSCWO* at a given fuel and oxidizer concentration? Under what conditions we can have the formation of hydrothermal flames at microscale? In the current work, we profoundly dwell on this problem using numerical analysis and seek understanding of the factors leading to such an observation, which can be further be used for better experimental work and technological development.

3. Model and physical parameters

3.1. Governing equations

The governing equations solved are the conservation of mass, momentum, energy, and species for a compressible flow [39–41]. Pressure is calculated using Peng-Robinson equation of state to account for real-gas effects as are prevalent in high pressure systems. While details of the model can be found in the aforementioned references, a brief summary is given in supplementary information. The governing equations are written as:

Conservation of mass:

$$\frac{\partial \rho}{\partial t} + \nabla.(\rho \boldsymbol{V}) = 0 \tag{1}$$

Conservation of species:

$$\rho\left(\frac{\partial Y_k}{\partial t} + \boldsymbol{V}.\nabla Y_k\right) = -\nabla \bullet \left(\rho Y_k \boldsymbol{V}_k^{(d)}\right) + \dot{\omega}_k, k = 1 to N \tag{2}$$

Here, Y_k, $\boldsymbol{V}_k^{(d)}$ and $\dot{\omega}_k$ denote species mass fraction, diffusion velocity, and rate of formation/consumption of k^{th} species, respectively. In the current work, we assume Fick's law of diffusion as given in [42] which reduces $Y_k \boldsymbol{V}_k^{(d)} = -D_k \nabla Y_k$.

The energy equation is solved in C_V (specific heat at constant volume) form and is given by:

$$\rho C_V\left(\frac{\partial T}{\partial t} + \boldsymbol{V}.\nabla T\right) = -T\frac{\beta_P}{\chi_T}\nabla \bullet \boldsymbol{V} + \nabla \bullet (k\nabla T) + \varphi + \dot{\omega}_T^{''} - \left(\rho \sum_{k=1}^{N} Y_k V_k^{(d)}\right).\nabla h_{s,k} - \sum_k (P_k/\rho_k)\left(\nabla \bullet \left(\rho Y_k V_k^{(d)}\right)\right) \tag{3}$$

Here, $\varphi = \tau_{ji}\frac{\partial u_i}{\partial x_j}$ is the viscous dissipation with τ_{ji} being the viscous stress tensor. Further, χ_T and β_P denote the isothermal compressibility and thermal expansion at constant pressure, respectively. The species sensible enthalpy $h_{s,k}$ is given by $h_{s,k} = h_{s,k}^0(T) + h_{s,k}^{(R)}$ where $h_{s,k}^{(R)}$ is the residual enthalpy representing the deviation from perfect gas conditions (see Eq. (7)) and $h_{s,k}^0(T)$ is evaluated from 7-point NASA polynomial form

[43]. The necessity to account for residual enthalpy arises because real fluid effects play an important role in the current operating conditions as also highlighted in [44]. Further, $\dot{\omega}_T^{''}$ represents the heat generated due to the formation/consumption of the species and is given by $\dot{\omega}_T^{''} = -\sum_{k=1}^{N} e_k(T)\dot{\omega}_k$. Here, $e_k(T) = e_{s,k}(T) + \Delta h_{f,k}^o$, with $e_{s,k}(T)$ being the sensible internal energy evaluated using the expression $e_{s,k}(T) = \int_{T_{ref}}^{T} C_V dT + e_{s,k}(T_{ref}) + U_k^{(R)}$ where $U_k^{(R)}$ is the residual internal energy (see Eq. (8)). $e_{s,k}(T_{ref})$ denotes the reference internal energy evaluated as $e_{s,k}(T_{ref}) = -\frac{RT_{ref}}{W_k}$ with $T_{ref} = 298.15K$.

Conservation of momentum:

$$\rho\left(\frac{\partial \boldsymbol{V}}{\partial t} + \boldsymbol{V}.\nabla\boldsymbol{V}\right) = -\nabla P + \nabla.(\mu\nabla\boldsymbol{V}) + \nabla((\lambda+\mu)\nabla.\boldsymbol{V}) \tag{4}$$

The above equation is written in the absence of any external force such as gravity. λ and μ represent second and first coefficient of viscosity, respectively and here we have used Stokes hypothesis $\lambda + \frac{2}{3}\mu = 0$ to evaluate λ. This classical form is modified to incorporate the dependence of pressure on density and temperature directly into the momentum equation (See [41,45] and supplementary information for more details).

Finally, to close the model, we calculate pressure using Peng-Robinson cubic equation of state as follows,

$$P = \frac{RT}{\bar{v} - b_m} - \frac{\bar{a}_m}{(\bar{v} + \delta_1 b_m)(\bar{v} + \delta_2 b_m)} \tag{5}$$

where, $\delta_1 = 1+\sqrt{2}$ and $\delta_2 = 1-\sqrt{2}$, and $\bar{v}$ is the molar volume. The parameters $\bar{a}_m$ and b_m are evaluated using van der Waals mixing rules given by $\bar{a}_m = \sum_i^N \sum_j^N X_i X_j \bar{a}_{ij} = \sum_i^N \sum_j^N X_i X_j (1-k_{ij})(\bar{a}_i \bar{a}_j)^{1/2}$ and $b_m = \sum_{i=1}^N X_i b_i$. Here, X_i is the mole fraction and is related to mass-fraction as, $X_i = \frac{\frac{Y_i}{W_i}}{\sum_{i=1}^N \frac{Y_i}{W_i}}$. The binary interaction parameters k_{ij} are assumed to be zero and other parameters in Eq. (5) for individual species are evaluated as,

$$\bar{a} = a\alpha; a = 0.45723553\frac{R^2 T_c^2}{P_c}$$

$$\alpha = \left(1 + \kappa\left(1 - \sqrt{T_r}\right)\right)^2, T_r = T/T_c$$

$$\kappa = 0.37464 + 1.54226\omega - 0.26992\omega^2 \tag{6}$$

Here, ω is the acentric factor of the species and $b = 0.07779607\frac{RT_c}{P_c}$. The residual enthalpy and internal energy in Eq. (3) are evaluated using Peng-Robinson equation of state (Eq. (5)) using the following expression:

$$h_k^{(R)} = \frac{1}{W_k}\left(P_k\bar{v}_k - RT + \frac{(\bar{a}_k' T - \bar{a}_k)}{b_k(\delta_1 - \delta_2)}\left(\ln\frac{\bar{v}_k + \delta_1 b_k}{\bar{v}_k + \delta_2 b_k}\right)\right) \tag{7}$$

$$U_k^{(R)} = \frac{1}{W_k}\left(\frac{(\bar{a}_k' T - \bar{a}_k)}{b_k(\delta_1 - \delta_2)}\left(\ln\frac{\bar{v}_k + \delta_1 b_k}{\bar{v}_k + \delta_2 b_k}\right)\right) \tag{8}$$

Here, $P_k, \bar{v}_k = W_k/\rho Y_k$, $\bar{a}_k' = \frac{d\bar{a}_k}{dT}$ and b_k correspond to the parameters of the individual species. The properties χ_T and β_P are evaluated using their respective relation as $\chi_T = \frac{1}{\rho}\left(\frac{\partial\rho}{\partial P}\right)_T$ and $\beta_P = -\frac{1}{\rho}\left(\frac{\partial\rho}{\partial T}\right)_P$ from Peng-Robinson equation of state.

3.2. Thermophysical properties

An important aspect in high pressure simulations involving several species is implementing thermophysical properties such as viscosity, thermal conductivity, and specific heat. In the present work, properties for various species (viscosity and conductivity) are evaluated using a piecewise polynomial fit at a constant pressure of $25MPa$ (corresponding to the operating conditions) for the temperature in the range $300K < T < 1500K$. This range is chosen based on expected range of temperature during the SCWO/hydrothermal flames. The use of constant pressure can be justified as the expected pressure change would be very small in comparison to the operating pressure ($25MPa$) owing to flow at microscale. The relations for individual species are provided in supplementary information. The properties used for obtaining a piecewise polynomial fit were originally obtained using the method of Chung *et al.* [46] as well as NIST database [47] and subsequently piecewise relations as described in supplementary information were developed. The mixture viscosity and conductivity is calculated using the Wilke Method [48] as suggested for high pressure combustion in [49] and can be defined as (represented here for μ).

Table 1
Relevant data required for solving the governing equations.

Species	T_c [K]	P_c [MPa]	ω	M [kg/mol]	Δh_f^0 [kJ/mol]
EtOH	516.25	6.39	0.644	46.07	−234.95
O_2	154.6	5.05	0.025	32.00	0.0
CO_2	304.1	7.38	0.239	44.0	−393.51
H_2O	647.0966	22.064	0.344	18.0	−241.81

$$\mu = \sum_{k=1}^{N} X_k \phi_k \mu_k, \phi_k = \sum_{l=1}^{N} \Phi_{kl} X_l \tag{9}$$

$$\Phi_{kl} = \frac{\left[1 + (\mu_k/\mu_l)^{1/2}(W_k/W_l)^{1/4}\right]^2}{\left[8\left(1 + \left(\frac{W_k}{W_l}\right)\right)\right]^{1/2}} \tag{10}$$

The specific heat of the mixture required in energy equation is defined by $C_V = \sum_{k=1}^{N} C_{V,k} Y_k$. Here, the individual species $C_{V,k}$ is calculated as the sum of ideal gas specific heat $C_{V,k}^{(ig)}$ and residual $C_{V,k}^{(R)}$. The former is obtained using $C_{V,k} = C_{P,k} - R/W_k$ with $C_{P,k}$ obtained from 7 point NASA polynomial form [43]. The latter is evaluated using $C_{V,k}^{(R)} = \left(\frac{\partial U_k^{(R)}}{\partial T}\right)_{\bar{v}}$. A comparison of specific heat at constant volume is also shown in supplementary information.

The diffusion coefficient in Eq. (2) representing the Fick's diffusion coefficient is given by the following expression [42]:

$$D_k = \frac{7.4 \times 10^{-8}(\beta_w W_w)^{1/2} T}{\mu_w V_{b,k}^{0.6}} \tag{11}$$

Here, β_w is the association factor having a value 2.6 for water solution, W_w and μ_w denote the molecular weight and viscosity of water, respectively. $V_{b,k}$ represents the molar volume at the boiling point of i^{th} species and is obtained in terms of critical volume of the species using $V_{b,k}^{0.6} = 0.285 V_{c,k}^{1.048}$. The species formation/consumption rate is given by $\dot{\omega}_k = W_k \nu_k \mathscr{C}$, where $\nu_k = \nu_k^{''} - \nu_k^{'}$ with $\nu_k^{'}$ and $\nu_k^{''}$ denoting reaction coefficients and W_k is the species molar mass. In the current work, we consider a single step irreversible reaction for the oxidation of ethanol (which also acts like a fuel) described in [42],

$$C_2H_5OH + 3O_2 \rightarrow 2CO_2 + 3H_2O \tag{12}$$

with reaction rate given by,

$$\mathscr{C}_{EtOH} = -10^{17.23}\exp\left(\frac{-E_a}{RT}\right)[EtOH]^{1.34}[O_2]^{0.55} \tag{13}$$

The activation energy in the above expression is, $E_a = 214\frac{kJ}{mol}$ [42]. Other relevant physical parameters used in the simulation are presented in Table 1.

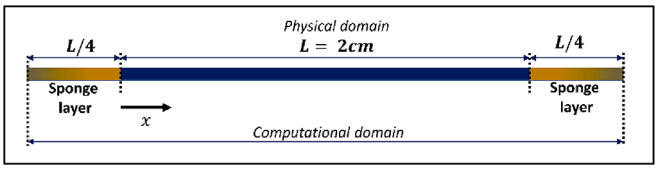

Fig. 5. Schematic of the validation case.

3.3. Numerical modeling

The above presented model along with the thermophysical properties are solved numerically using in house CFD code NOTUS [50,51]. The discretization of all the equations follows the classical finite volume method approach and has been discussed in supplementary information in more detail. The temporal terms are discretized using forward first order Euler scheme while the implicit second order central differencing is used for the advection and diffusion terms in the momentum and energy equation. The advection and diffusion terms in the species equations are discretized using explicit central difference and TVD superbee [52], respectively. The species generation/consumption rate $(\dot{\omega}_k)$ is treated explicitly and is added as a source term in the respective species equation. Further, we solve for *N-1* species and the mass fraction of last species (base/inert species – water in the current case) is adjusted to account for any deviations that may arise due to the assumption of Fick's law in a multicomponent system. An important aspect in open compressible flows are the boundary conditions, in particular the outlet condition wherein it is common to encounter reflection of the pressure waves from the boundary. A well-established approach to overcome this problem is to use Navier Stokes characteristic boundary conditions (NSCBC) [53]. An alternate approach is the use of sponge layer (which acts as a damping medium for the pressure waves being reflected from the boundaries, primarily at outlet) [54–56]. In the present case, the latter approach is followed owing to its simplicity in implementation as well as low Reynolds number regime in the present work. The effect of sponge layer is mathematically incorporated by adding the term $-K(V^{(n+1)} - V_{ref}^{(n)})$ in the momentum equation. $V_{ref}^{(n)}$ is defined as the average velocity near the boundary at the previous iteration. This is to ensure that velocity gradient tends to zero and pressure waves are damped. K denotes the strength of the sponge layer given by $K = K_0(|x - x_c|)^3/l^3$ as considered in [55], where x_c denotes the coordinate of the physical domain and l is the length of sponge layer taken to be $L/4$ in the present case. Further, K_0 denotes the coefficient of sponge layer. The current form ensures a smooth transition of enforcing the V_{ref} in the sponge layer of the computational domain.

4. Model validation

Though the above presented model has been validated for various test cases [41,45,57], it is being used for the first time to capture the reaction/combustion dynamics. Thus, we validate the model with a simple test case of a freely propagating premixed flame in 1D configuration as presented in [58]. The computational domain consists of a physical domain and a sponge layer as shown in Fig. 5, the latter acting as means of damping the pressure waves. A single step irreversible reaction defined by $C_3H_8 + 5\ O_2 \rightarrow 3\ CO_2 + 4\ H_2O$ is considered with reaction rate governed by $\omega = k.C_{C_3H_8}.C_{O_2}.e^{-\frac{E_a}{RT}}$ where $k = 9.9 \times 10^{13} cm^3 mol^{-1} s^{-1}$, $E_a = 30 kcal/mol$ and C_i denote molar concentration of i^{th} species. Here, the governing equations as presented above are solved assuming perfect gas and thus, pressure is evaluated using $P = \rho\left(\frac{R}{W}\right)T$. The various thermophysical properties, namely viscosity, conductivity, and species diffusion coefficients are evaluated using relations given in [58]. These have been presented in supplementary information for the sake of completeness. The flame speed is evaluated using the relation $S_L = U_f - \frac{\rho_f U_f - \rho_b U_b}{\rho_f - \rho_b}$ as given in [58] and is compared to the one presented in literature. Here, the subscript f and b respectively denote fresh and burnt gas properties which are evaluated at the starting and last point of the physical domain. The test case is presented here for only for one equivalence ratio $(\varnothing = 1)$ for the sake of conciseness. A short discussion on the choice of sponge layer is presented in supplementary information.

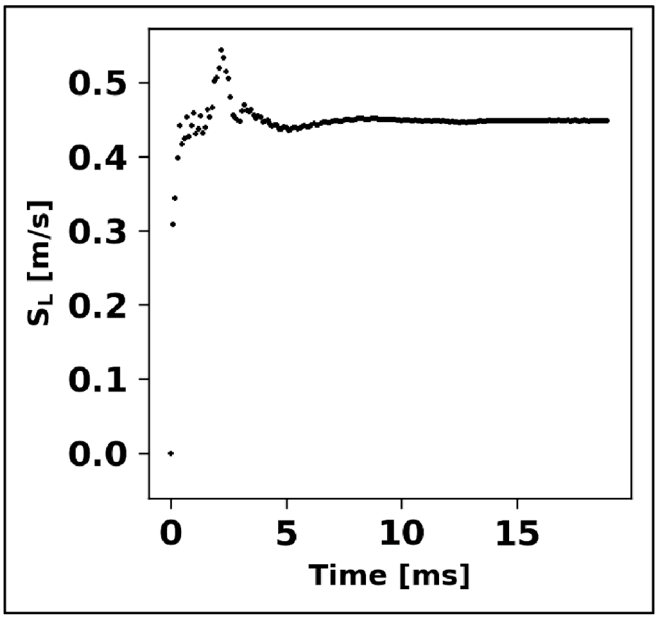

Fig. 6. Flame speed evaluated for premixed combustion for equivalence ratio = 1 as per conditions in [58].

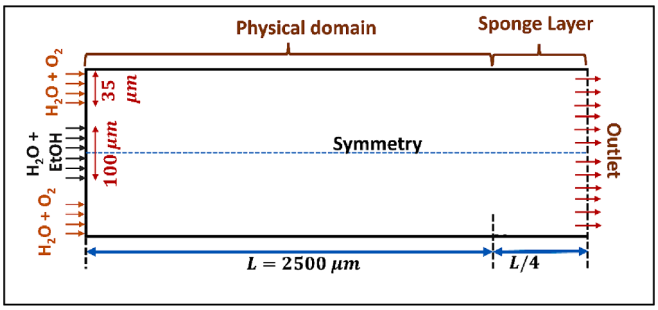

Fig. 7. Schematic of computational and physical domain.

Fig. 6 compares the evolution of flame speed over a period time and we observe the flame reaches a constant speed of 0.45 m/s. This is slightly less than the reported value of $0.5 m/s$ in the literature resulting in an error of 10%. This may be attributed to the difference in the formulation of the energy equation in the literature which is based on constant C_P (specific heat at constant pressure). However, the current model works with C_V formulation, which varies across the domain due to the relation $C_V = C_P - R/W$ with W (mixture molar mass) varying in space. This may lead to a slightly different behavior than at a constant C_P formulation as presented in the literature. Nevertheless, the developed model is able to capture the propagation of flame propagation within acceptable limits of error and thus is extended to study hydrothermal flames at microscale in the present work.

5. Problem description

Fig. 7 shows the physical and computational domain used in the current work. The dimensions considered in the present work are in

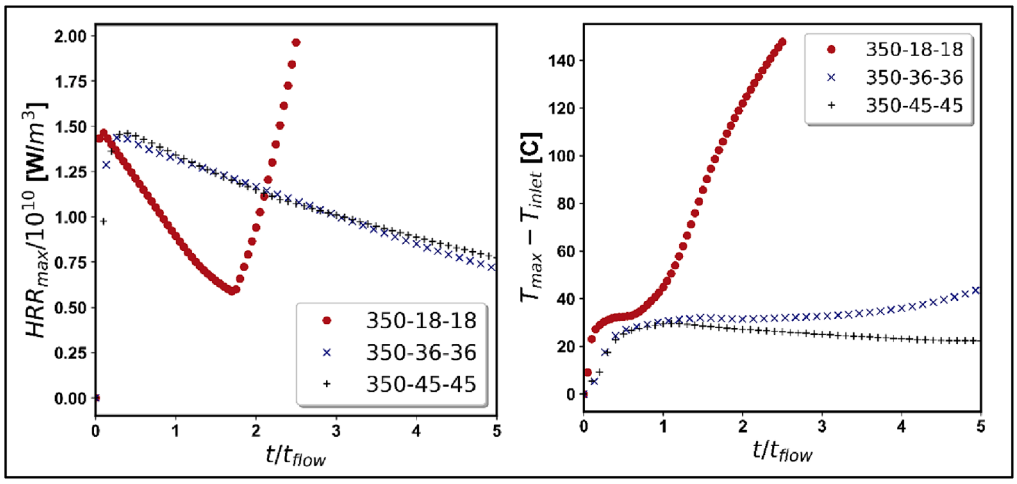

Fig. 8. Maximum heat release and maximum temperature in the domain for $T_{inlet} = 350C$ at different flow velocities. (For the sake of conciseness, the operating conditions are henceforth denoted as per the legend $T_{inlet} - V_f - V_o$, for example $350 - 18 - 18$ implies $T_{inlet} = 350C, V_f = 18mm.s^{-1}, V_o = 18mm.s^{-1}$).

coherence with physically realizable system for $\mu SCWO - H$ [35]. The length of microreactor is $2500\mu m$ while the inlet of fuel (injected at the center) is $100\mu m$. The oxidizer (oxygen) is injected through the outer channel with size being $65\mu m$ each side. To save computational time, only half the domain is solved and symmetry is imposed as highlighted in Fig. 7. The sponge layer is added at the exit with $K_0 = 10^9 - 10^{12}$, the choice based on arguments explained in supplementary information for the validation test case.

The behavior of hydrothermal flames is investigated primarily for two inlet temperatures, $T = 350C$ and $T = 365C$. This motivation lies in analyzing the system in subcritical conditions w.r.t the critical point of water due to the following reasons. Firstly, injecting the reactants at a lower temperature (subcritical) result in the increased process efficiency in terms of energy requirement and secondly, it impedes the precipitation of the salts as mentioned previously. The initial system pressure is held at $25MPa$ while the initial temperature corresponds to the inlet temperature. This is in coherence with the physical system at microscale wherein heating the microreactor is expected to yield a homogeneous temperature of the fluid at the inlet as well as in the main reactor channel. The fuel (ethanol) and oxidizer mass fraction is fixed at 4.3% and 9%, respectively, as considered in premixed configuration by Koido *et al.* [42] and the focus of the current work is primarily to investigate the influence of flow rates on the formation of hydrothermal flames. The range of flow velocities vary from $9mm/s$ to $72mm/s$ resulting in the Reynolds number $(Re = \rho_{in} U_{in} d/\mu_{in})$ varying from 6 to 72, where subscript *"in"* refers to the properties at the inlet. Since the simulations are transient in nature, final time to reach steady state is not known apriori. In order to abstain from running long simulations, the behavior of the flames is analyzed till 5 flow times (*i.e.*, $t_f = L/\min(V_f, V_o)$). Initially, the microreactor is filled with water at aforementioned conditions while fuel and oxidizer are injected therein. The simulations are performed using a time step $dt = 0.5\mu s$. The grid independent study was performed using the following grid sizes of $2.5\mu m \times 4\mu m, 2\mu m \times 2.5\mu m$, and $1\mu m \times 2\mu m$ and the maximum heat generated in the system was compared. Very less difference was observed when moving from grid size $2\mu m \times 2.5\mu m$ to $1\mu m \times 2\mu m$ and thus all the simulations were performed using the $2\mu m \times 2.5\mu m$ grid size.

6. Results and discussions

The following sections present the key findings in the following order. Firstly, we seek to identify the flow rates for which the oxidation reaction can be categorized as ignition (hydrothermal flame). We then proceed to explain why these identified flow rates result in formation of flames followed by understanding their key characteristics. An analysis at two different aforementioned temperatures highlights the differences between the flame structure when approaching the critical point of water.

6.1. $\mu SCWO$ or. $\mu SCWO - H$

In order to distinguish between the SCWO with or without hydrothermal flames, an appropriate criterion needs to be defined. Since the hydrothermal flames are formed due to autoignition, a similar condition in other autoignition systems such as ignition delay in diesel engines can be sought. However, this in itself has been a subject of ambiguity, both in experimental and computational studies. Several definitions have been used by various authors, such as detection of light emission by a photocell during experiments, increase in temperature due to combustion, rapid increase in gas temperature and reaction rate, increase in the average temperature of the combustion chamber by 1 % [59–62]. Owing to the nature of hydrothermal flames, which is also termed as cold combustion, a very large increase in temperature may not be apt to define the criterion. A pressure-based condition is ruled out owing to microscale operation as the expected pressure rise is quite small when compared to the operating one. In the current work, we opt for maximum *HRR* (heat release rate) in the domain to identify the autoignition and is shown for various flow rates in Fig. 8 (For the sake of conciseness, the operating conditions are henceforth denoted as per the legend $T_{inlet} - V_f - V_o$, for example $350 - 18 - 18$ implies $T_{inlet} = 350C$, $V_f = 18mm.s^{-1}, V_o = 18mm.s^{-1}$). A common feature in all the cases is the uniform increase in HRR_{max} for some initial period which represents the initial reaction between ethanol and oxygen when they come in contact with each other. This is the simple oxidation period. This can be justified as the formation of hydrothermal flames due to autoignition is bound to be preceded by an oxidation reaction. Now the question is whether this oxidation reaction will sustain itself as it is or eventually lead to autoignition. Thus, emphasis lies on analyzing what happens after this initial phase of reaction. Based on HRR_{max} plot, three different trends can be identified for both the operating temperatures considered in this work. We discuss these for $T_{inlet} = 350C$ and similar reasoning holds for the other case. The first regime is where HRR_{max} starts to decrease followed by its sudden increase while T_{max} in the domain is increasing, as in the case of $350 - 18 - 18$ in Fig. 8.

From a technological and process perspective, this is the regime we intend to have and thus will be discussed in more detail in subsequent sections. We define this regime as hydrothermal regime owing to sudden change in the slope of HRR_{max} denoting autoignition. The second regime

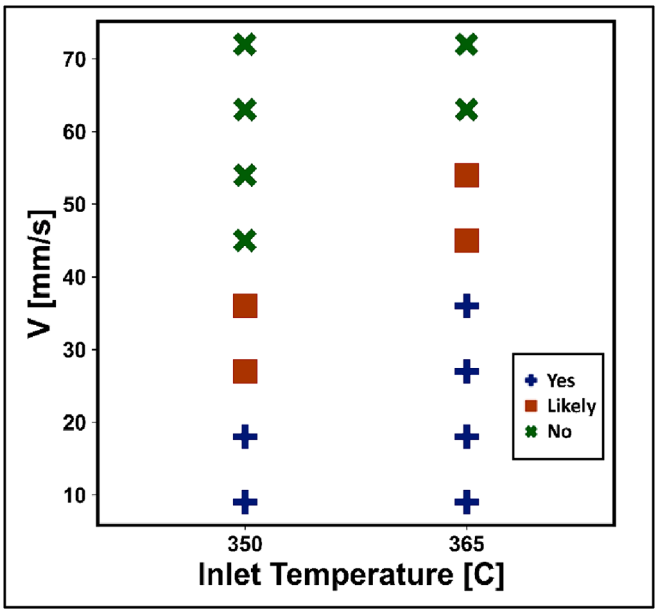

Fig. 9. Ignition map in terms of flow velocities for two different inlet temperatures.

corresponds to the case illustrated for 350 −45 −4 5 where both the HRR_{max} and T_{max} are decreasing with time and we characterize this regime as a simple SCWO regime as over a period of time, this is expected to attain a stationary thermodynamic state. The third regime is identified wherein HRR_{max} is decreasing while T_{max} in the domain is increasing, for instance in 350 −27 −27. We term this condition as likely-flame to preclude the possibility of missing out hydrothermal regime due to limited computational time considered in the present work. This implies that had the simulation been run for a longer time, there lies a possibility to have ignition or the temperature may have started to decrease as in the case of regime 2. Based on the above defined criterion, an ignition map is drawn for different velocities considered and is shown in Fig. 9. The following two inferences can be made from the ignition map. Firstly, a higher flow velocity does not favor the formation of hydrothermal flames at microscale in the current physical setup and secondly, with increase in temperature, there is an increase in the permissible flow rates leading to the formation of hydrothermal flames. In order to elucidate the observed behavior, we now discuss the formation and dynamics of hydrothermal flames.

6.2. Dynamics of hydrothermal flames

We divide the dynamics of hydrothermal flames into two parts, the formation of ignition kernel, and flame structure and propagation. The former will aid in understanding the trend presented in Fig. 9 while the latter is primarily targeted to understand the flame characteristics which can eventually be used to improve upon the physical process. We start by defining two important parameters used to understand non-premixed flames, namely, mixture fraction (Z) and scalar dissipation rate (χ). The former is given by [63,64]

$$Z = \frac{[sY_F - Y_o]_M - [sY_F - Y_o]_o}{[sY_F - Y_o]_F - [sY_F - Y_o]_o}, s = \left(\frac{Y_o}{Y_F}\right)_{st} = \frac{\nu_o W_o}{\nu_F W_F} \tag{14}$$

Unlike the most usual diffusion flame configurations, where the fuel stream consists only of fuel yielding $Y_{F,F} = 1$, in the present case $Y_{F,F}$ and $Y_{o,o}$ correspond to the fuel and oxidizer mass fraction at the inlet with $s = 2.08$ and $Z_{st} = 0.5015$. Here, the subscript st denotes stoichiometric. The second parameter, scalar dissipation is defined by $\chi = D_{th}(\nabla Z)^2$, where D_{th} is thermal diffusivity.

6.2.1. Formation of ignition kernel

The prime objective of this section lies in understanding why autoignition (regime 1 in Fig. 9) is observed only for certain flow rates. Consider the hydrodynamics of co-flow configuration where the height (or the length) of the jet, termed as distance from the inlet to the tip of the jet, is known to depend on the volumetric flow rate or flow velocity at a given inlet temperature (for co-axial laminar flame, $L_f \propto \frac{Q}{D_{eff}}$, where Q is volumetric flow rate and D_{eff} is effective species mass diffusion coefficient [65,66]). It is to be mentioned that despite autoignition not present in all the cases, the relation described above can be considered valid owing to the omnipresence of the oxidation reaction and thus heat generation in the reaction zone. To avoid ambiguity, we use reacting mixture henceforth for a general case and flame is referred only for cases where autoignition is observed. Owing to microscale of operation, it can be ascertained that depending on the flow velocities, the length of reaction zone jet could be smaller/larger than the physical dimensions of the reactor itself. In order to further elucidate the observed trends, let us consider one case, 350 −18 −18, for which tip of the jet lies within the physical domain. With downstream advection of the heat generated in the reaction zone in conjunction with its concavity focuses heat ahead resulting in the formation of a high temperature zone, primarily near the tip of the jet. In this region, we have two competing phenomena which govern the overall behavior. Firstly, the flow of heat towards a relatively low temperature zones, mainly upstream as well as towards the core of the jet as illustrated in schematic of the phenomenon (Fig. 10 (a)). This behavior can be described as heat focusing. The second phenomenon is

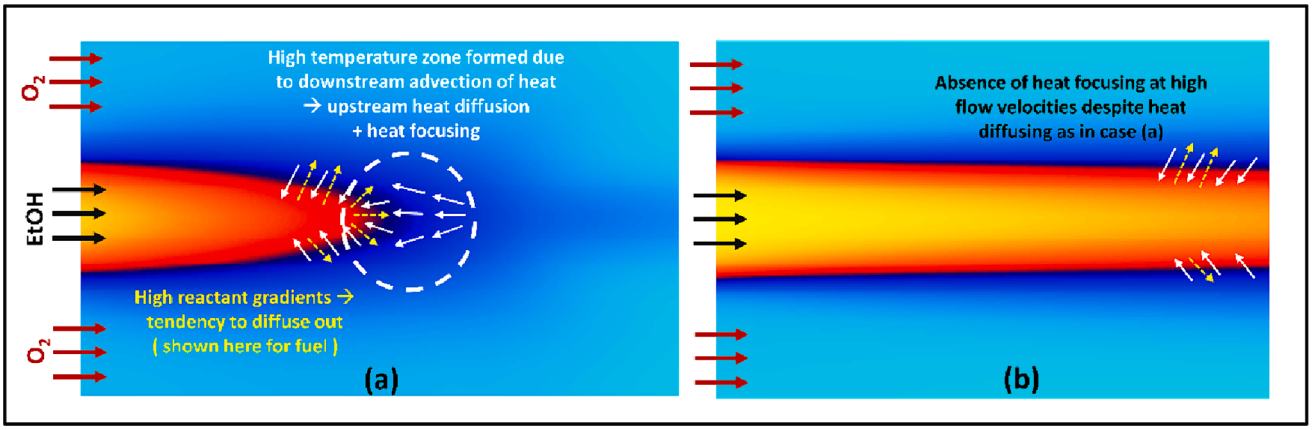

Fig. 10. Schematic of phenomenon leading to autoignition at low rates (case (a)) and absence of autoignition at high flow rates (case (b)).

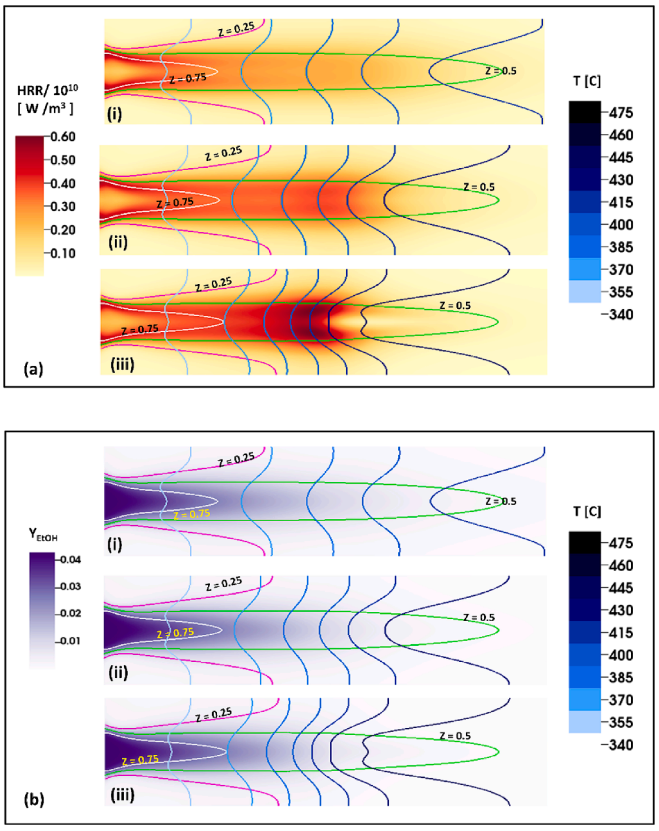

Fig. 11. Contour plots (filled) of *HRR* (a) and ethanol mass fraction (b) along with contour lines of temperature and mixture fraction (lines with values marked). The figure illustrates chain of events leading to formation of ignition kernel (visible as zone of high *HRR* in (iii)) for case 350 −18 −18. The $y-axis$ has been scaled by a factor of two for better visualization.

the diffusion of the fuel (ethanol) out of the reaction zone towards the oxidizer side owing to a higher concentration gradient in the reaction zone. A similar behavior can be ascertained for the oxygen to diffuse into the fuel side. While it is intuitive to expect that this heat focusing will increase the temperature thereby increasing the reaction rate, the latter phenomenon will depend on sufficient availability of the reactants, primarily fuel, to increase the reaction rate.

Thus, there exists a competition between the two effects and dominance of either, heat diffusion (focusing) or species diffusion, will govern the overall behavior. This can be characterized in terms of Lewis number which defines the ratio of thermal to mass diffusion. In the current case, Le_{EtOH} defined as $\frac{D_{th}}{D_{EtOH}}$, where D_{th} is the thermal diffusivity $O(10^{-7})$ while D_{EtOH} is mass diffusivity of ethanol $O(10^{-8})$, results in Le_{EtOH} 1.5 −3 in the computational domain. Thus, a relative faster heat diffusion causes increase in the reaction rate before the fuel diffuses out leading to temperature increase which further creates zone of a higher temperature. The phenomenon is thus similar to diffusional stratification as explained in [67]. This cyclic chain of events eventually results in the attainment of autoignition conditions resulting in the formation of ignition kernel. Thus, the shape of jet arising due to hydrodynamics in conjunction with the heat focusing can be identified as the prime reason for the autoignition in the current configuration. This is presented in Fig. 11(a) for the case 350 −18 −18 at various time instances just before formation of ignition kernel. For sake of better understanding contours of fuel (ethanol) are also shown in Fig. 11(b). In case of relatively high flow rates, even though heat is being diffused into the fuel side as illustrated in Fig. 10(b), the net effect of focusing is too weak to increase the temperature and thus unable to initiate autoignition which explains the observance of regime 2 in Fig. 9. Another observation which needs to be addressed is the extension of permissible flow rates for autoignition at higher initial temperature ($T = 365C$), regime 1 is extended to higher flow velocities. With a higher initial temperature, a higher heat release can be ascertained during the reaction and thus the net heat focusing effect will be stronger for the similar flow velocity when compared with a lower initial temperature. This explains regime 1 extending to higher inlet velocities as observed for $T = 365$ C though beyond a certain threshold velocity, no autoignition occurs as in the case of $T = 350C$. A similar reasoning for the autoignition will hold true for the case of open jet with concavity away from the axis.

Based on the above explanation, a regime 3 was also defined for the flow rates for which it is not completely certain that which of the two aforementioned phenomena would end up dominating. We thus categorize this intermediate regime as a transition regime and define it as the likely-flame regime. It is thereby evident that autoignition for hydrothermal flames at microscale in the current system is governed by the physical dimension of the system. This further highlights the technological challenge associated with $\mu SCWO-H$. It is to be mentioned that the current analysis may present a notion that all low flow rates may lead to autoignition, and there only exists an upper limit with no lower bound. However, this may not be true in physical scenarios where very low flow rates may not yield enough mixing or unfeasible ignition kernel formation location in the channel (discussed below) to cause autoignition.

Before moving further, we would like to highlight an important parameter related to formation of the ignition kernel – the ignition delay time (τ_{igd}) defined as the time taken by the reacting mixture to auto-

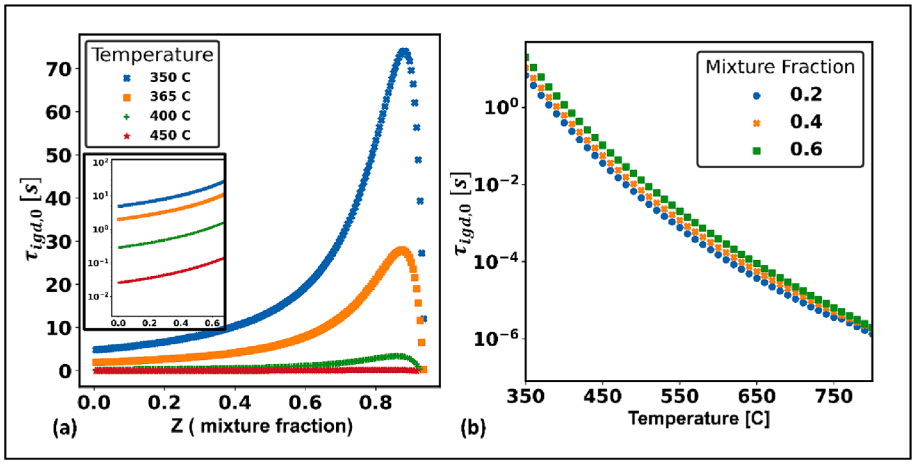

Fig. 12. (a) $\tau_{igd,0}$ vs mixture fraction for $T = 350C$ and $T = 365C$ (b) $\tau_{igd,0}$ for a wide range of temperature for various mixture fraction.

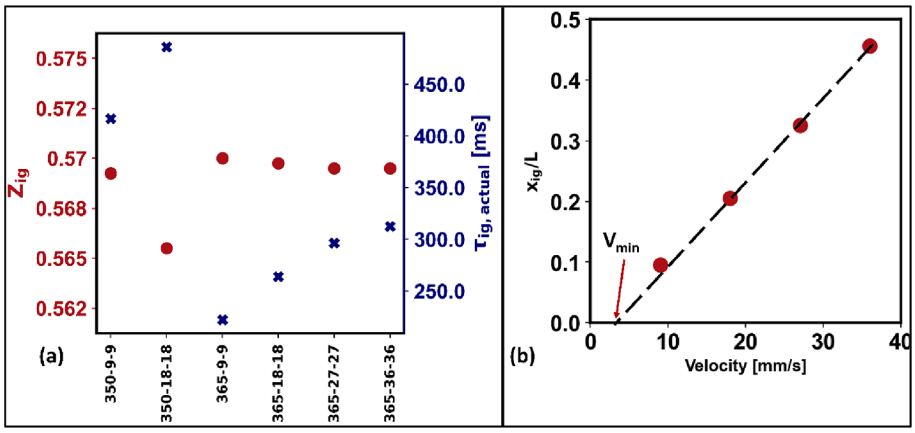

Fig. 13. (a) Mixture fraction at the formation of ignition kernel and actual ignition delay time as observed from simulations (b) dimensionless distance of formation of ignition kernel along $x-$ axis for $T_{in} = 365^{\circ}C$.

ignite. An initial estimate of τ_{igd} can be obtained from homogeneous mixing ignition calculations, *i.e.* solving the governing equations only in time whilst neglecting any diffusion effects. The corresponding ignition delay time is denoted by $\tau_{igd,0}$. Each case in the homogeneous calculation can be thought of as a reacting element secluded from its surrounding elements. The motivation of such an analysis arises to seek insights into the potential regions in the mixture fraction space where we can expect the formation of the ignition kernel. This is possible by identifying the mixture fraction for which $\tau_{igd,0}$ is minimum and has been defined as the most reactive mixture fraction (Z_{MR}) by Mastorkas *et al.* [64]. In their work, the authors demonstrated that $\tau_{igd,0}$ versus Z curve was a V shaped curve from which Z_{MR} can be obtained. However, in a few recent works [30,31,44], it is shown that this is not always true and in certain cases, such as hydrothermal flames using hydrogen as a fuel, more than a single minimum can exist resulting in the absence of a unique Z_{MR}. Nevertheless, such a curve can provide insight into the likelihood of the mixture fraction along which the ignition kernel may be formed. On similar lines as in [64,68,69], we seek insights into the trend of $\tau_{igd,0}$ w.r.t Z for different temperatures and operating pressure of 250*bar*. The initial concentrations are derived as described in [64,70] using the following relation,

$$Y_{EtOH} = Y_{EtOH,fu}Z \tag{15}$$

$$Y_{O_2} = Y_{O_2,o}(1-Z) \tag{16}$$

Here, $Y_{EtOH,fu}$ and $Y_{O_2,o}$ denote the concentration of fuel and oxygen at the inlet. The above transformation thereby facilitates to map the mixture fraction to ignition delay time for a given pressure and a temperature. Fig. 12(a) shows $\tau_{igd,0}$ for four different temperatures, two of them corresponding to the inlet temperatures considered in the present work. While the trend shows to have a maximum as was also observed in [31,44], there is no distinct minima. This behavior can be ascribed to a single step reaction considered in the present analysis. Nevertheless, it can be seen that the ignition delay time reduces significantly on increasing the temperature while it peaks around $Z\,0.85-0.8\;8$. Furthermore, the curves seem to become flatter on the lean side with increase in temperature. For better estimation of order of magnitude, the time axis is also shown on log scale in inset of Fig. 12(a). It can thus be ascertained that relatively low mixture fractions $Z < 0.6$, *i.e.* of the order of stoichiometric mixture fraction are most likely to be ignited first. A further comparison for different mixture fractions over a wider range of temperatures is also shown in Fig. 12(b) to illustrate in a better way the large variation in time scales of $\tau_{igd,0}$ (nearly 5 order decrease with $300^{\circ}C$ increase in temperature).

We further plot the mixture fraction at which the ignition kernel is initially formed (*i.e.* Z where we have HRR_{max} at the time of ignition) for the relevant cases (regime). This is shown in Fig. 13(a) and it can be observed that the values lie in the range of $0.56-0.58$ which implies that the ignition kernel is formed in a slightly fuel rich region but not very far away from Z_{st}. We also plot the actual ignition delay time, *i.e.* time after which autoignition is observed in simulations $(\tau_{igd,simu})$ in Fig. 13(a). The initial observation is that $\tau_{igd,simu}$ is significantly lower than $\tau_{igd,0}$ corresponding to inlet temperature conditions. However, it is to be noted that autoignition conditions are attained after successive increase in local temperature due to heat focusing and thus the next effective ignition delay is the consequence of ignition delay times encountered at all the relevant conditions (mixture fraction and temperature). On further inspection, it is observed that temperature at the instance of formation of ignition kernel (*i.e.* location where we have HRR_{max}) is in the range of $415-420\,C$ for all the cases. $\tau_{igd,0}$ in these relevant conditions is nearly the same order $(O(ms))$ as $\tau_{igd,simu}$. Another observation is that $\tau_{igd,simu}$ decreases with an increase in the inlet temperature but varies inversely with flow rate. While the former observation is intuitive to explain - a higher inlet temperature entails a higher reaction rate and thus a smaller time is required to attain autoignition, the latter can be ascribed to a higher heat advection at higher flow rates. Thus, in contrast to turbulent flows where a higher flow velocity may result in a better mixing and thus reduction in the ignition delay time, the mixing in the current case is primarily driven by molecular diffusion owing to laminar regime and thus the effect of increase in the flow rate is predominantly observed in the advection of heat rather than enhanced mixing. In addition, a higher flow velocity implies a lower heat focusing owing to a wider width of the jet which eventually results in a higher time required to attain autoignition conditions when compared to lower flow velocities.

Lastly, we seek insights into the distance from the inlet to the x coordinate where the ignition kernel is formed, x_{ig}. This can also be interpreted as the ratio of the advection time until autoignition $(\tau_{adv,ig})$ and one flow time, where we define $\tau_{adv,ig} = x_{ig}/V_{inlet}$. Since there are not enough data points for $T = 350^{\circ}C$, we have plotted x_{ig} only for the case of $T = 365^{\circ}C$ in Fig. 13(b), nondimensionalized by the length of the reactor channel. A monotonically increasing behavior with flow velocity is observed which is self-explanatory as a higher flow rate implies that a larger ignition delay time and thus the formation of ignition kernel being farther away from the inlet. It is interesting to note that when extrapolating this line backwards, we see that there is a minimum velocity $(2.3mm/s)$ at which the ignition kernel will be formed just at the inlet. Physically, this can be interpreted as follows - when the flow rate is so small that the tip of the jet is close to the inlet resulting in formation of the kernel just near the entrance zone. It can thereby be ascertained that just like there exists an upper limit on flow rates for the autoignition, there also exists a lower limit below which all the ignition kernels will

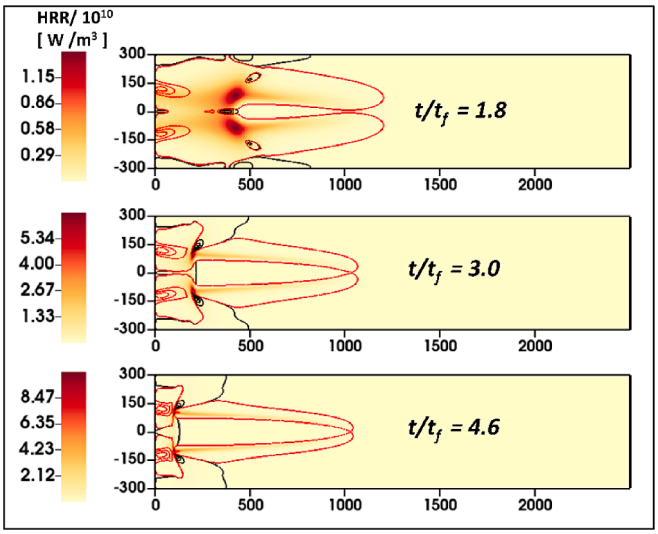

Fig. 14. Contour plots of *HRR* for 350 −9 −9 at different time instances post formation of ignition kernel. The solid lines represent flame index (see Eq. (17). The black lines denote positive values and thus premixed branches while red lines refer to negative values denoting diffusion branch. The $y-axis$ has been scaled by a factor of two for better visualization. (For interpretation of the references to color in this figure legend, the reader is referred to the web version of this article.)

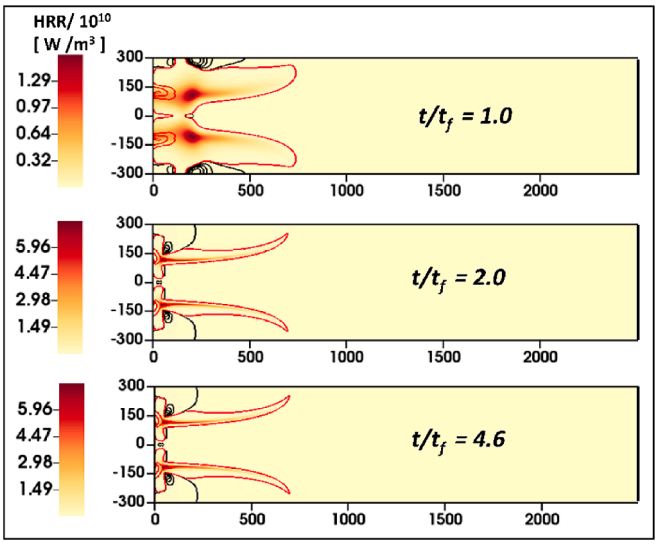

Fig. 15. *HRR*And*FI* plots for 365 −9 −9. The color code for *FI* is same as in Fig. 15.

stick close to the entrance which may not be desired from the current application perspectives under consideration. A similar plot can be drawn for other initial temperatures and conditions which can aid in providing the lower limit of flow rates to be considered in the real system.

6.2.2. *Flame characteristics: structure, shape, and propagation*

Upon the formation of the ignition kernel, the conditions in which the flame will propagate is a SCW medium. The medium is not only different from conventional perfect gas systems but is also dynamic in nature primarily due to large variations in the properties of SCW. In this section, we thus investigate some of the characteristics of the hydrothermal flame formed on similar lines as in case of conventional (ideal gas like or high pressure gaseous) non-premixed flames. These primarily include the dynamics after the formation of the ignition kernel. We firstly look at the structure of the flame. In most of the co-flow/co-axial diffusion flames, the flame structure is a typical triple flame in nature. This comprises two non-premixed branches and one diffusion branch [68,71,72]. In certain cases, as the flame evolves and stabilizes, this may become bi-branchial owing to local reaction chemistry as was shown by Song et al. [30]. In the current work, we investigate a similar behavior for two different inlet temperatures considered. It is well established that the ignition kernel is formed in a region of low scalar dissipation and thus corresponding to a small mixture fraction gradient ($|\nabla Z|$). Once formed, the heat conduction modifies the flow field, primarily upstream resulting in the reduction of mixture fraction gradient. Thus, the ignition kernel propagates from a region of low mixture fraction gradient to a higher one and expands in both the directions - *i.e.* towards the fuel side (fuel rich region) and oxidizer side (fuel lean region). In both these sides, as the stoichiometry departs significantly from unity equivalence ratio, different reaction rates persist in both these sides thereby resulting in different propagation speed of the reacting mixture in each side. Consequently, we have the formation of two premixed branches which curve in shape owing to different propagation speed. These two branches along with the initial diffusion region where the ignition kernel was formed meet at a common point, termed as the triple point [68] and are together known as the triple flame. In order to quantify this behavior more appropriately, a measure defined as the flame index (FI) was proposed by Yamashita et al. [73] which can be defined as,

$$FI = \nabla Y_F \bullet \nabla Y_o \tag{17}$$

A positive value of *FI* implies that both the gradients are in the same direction and thus denote the premixed branch while a negative value denotes diffusion branch. We plot contours of *FI* overlaid over the contours of *HRR* in the domain and this is illustrated for the case 350 − 9-9 in Fig. 14 for different time instances. It can be seen that in the early stages post formation of ignition kernel, the flame is primarily diffusive and with evolution in time, the premixed branches evolve. This is ascribed to the spreading of ignition kernel into both sides, fuel rich and fuel lean as defined previously, making the premixed branches more evident.

It is important to note that no quantitative conclusion can be made on the strength of the premixed branches relative to the diffusive branch from this index. Nevertheless, it highlights that the structure of the hydrothermal flame under investigation resembles tri-brachial structure. A similar observation is made for the case when the inlet temperature is 365 $^{\circ}C$ as illustrated in Fig. 15. Thus, it can be ascertained that under the given operating conditions, the co-flow configuration at microscale leads to the formation of classical tri-brachial flame.

We further analyzed *HRR* in the mixture fraction space to have more insights into the characteristics of presented hydrothermal flame. One such means is using conditional statistics as demonstrated for turbulent combustion, primarily $Z-$ conditional density averaged *HRR* [32,74]. The conditional statistic of *HRR* is defined as $HRR|Z_i$ and implies the value of *HRR* given the mixture fraction Z_i, where i varies from 0 to 1. As we are dealing with laminar regime, we evaluate this as an average over a region and define it as,

$$HRR_{cond} = \frac{\int HRR|Z_i dA}{\int 1|Z_i dA}, Z_j < Z_i < Z_{j+\Delta z} \tag{18}$$

Here, j varies from 0 to $(1-\Delta z)$ with $\Delta z = 0.01$. The numerator in Eq. (18) represents the summation of area weighted *HRR* for the region where $Z_j < Z_i < Z_{j+\Delta z}$ and the denominator implies the corresponding area and thus, HRR_{cond} denotes area averaged conditional *HRR*. The objective of such an analysis is to analyze how does the flame/reaction zone evolve over the entire domain over a period of time. We first compare HRR_{cond} for the same inlet temperature ($T_{in} = 350^{\circ}C$) for two different inlet flow velocities and this is shown in Fig. 16. It is observed that in the initial reaction phase, *HRR* is primarily concentrated in the

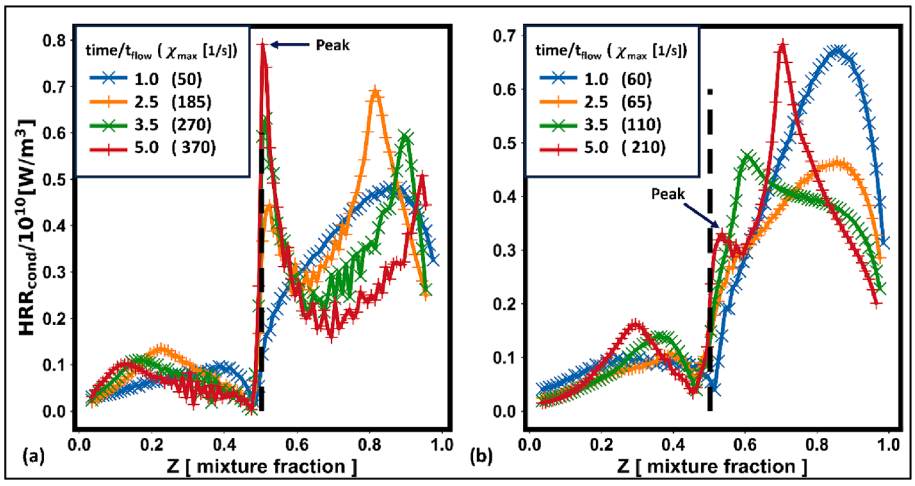

Fig. 16. HRR_{cond}For $T_{in} = 350C$ for inlet velocity of (a) 9 mm/s (b) 18 mm/s. The solid dashed line corresponds to Z_{st}. Approximate values of maximum scalar dissipation in the domain have also been marked at each time instance in the bracket.

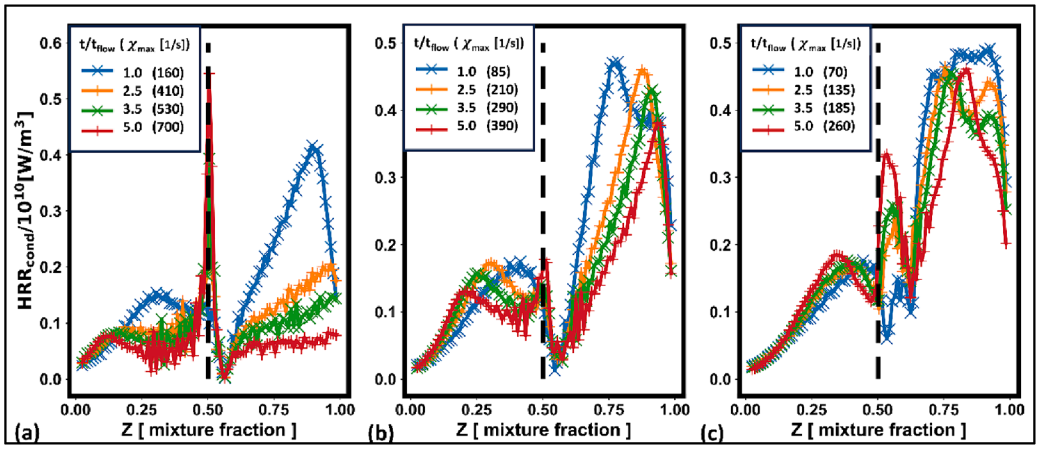

Fig. 17. HRR_{cond}For $T_{in} = 365C$ for inlet velocity of (a) 9 mm/s (b) 18 mm/s (c) 36 mm/s. The solid dashed line corresponds to Z_{st}. Approximate values of maximum scalar dissipation in the domain have also been marked at each time instance in the bracket.

fuel rich side of the reacting mixture. Once the ignition kernel is formed following which the flame develops and propagates, the diffusion and the two premixed branches become more evident as peaks appear in fuel rich and fuel lean region as well as near the stoichiometry value. The observation is thus in coherence with *FI* contours in Fig. 14. Furthermore, with increase in the inlet flow velocity, the peaks for the premixed branches shift towards the stochiometric value or towards the diffusion branch. This can be ascribed to the fact that a higher flow velocity entails a lower diffusion time along with a higher heat loss due to heat advection. This eventually leads to circumventing the spread of the ignition kernel deeper into the fuel rich and fuel lean region and thus the observed behavior. It is worth highlighting that lower intensity of HRR_{cond} in the diffusion regime at a higher velocity does not imply that the total strength of diffusion branch is smaller. This behavior arises as with increase in the flow velocity, the length of the diffusion branch increases while that of premixed branches would remain nearly the same. Thus, the area weighted average for diffusion branch would be lower as observed in Fig. 16. Nevertheless, the inference from the HRR_{cond} is restricted primarily for understanding the behavioral patterns of premixed and diffusion branch. A similar plot is illustrated for the inlet temperature of $365^{\circ}C$ for different flow velocities in Fig. 17. The trend is similar lines to the case of $T_{in} = 350^{\circ}C$, particularly in terms of peaks shifting towards the stoichiometry value. It can thereby be ascertained that at higher flow velocities, in case we are somehow able to attain hydrothermal flames, the tri-brachial structure may disappear over a period of time as the two premixed branches may merge with the diffusion branch. Another notable observation is that at a higher flow velocity, for both the cases of inlet temperatures, the peak in case of diffusion branch moves slightly towards the fuel rich region as highlighted for one case in Fig. 16 in the same non-dimensionalized time. This may be explained by the fact that as the ignition kernel is formed at a later time for a higher flow velocity, the flame has not evolved completely in the same time frame considered for simulation. Thus, high inlet velocity cases flames require larger multiples of flow time to evolve completely.

Having looked at the structure of the flame and its evolution in time, we further investigated the propagation characteristics of the flame. This is primarily important for understanding the flame stabilization which could further aid in providing an estimate of where flame would anchor itself. Depending on flow rates, the flame may anchor itself at the base *i.e.* near the inlet or somewhere downstream in the reactor microchannel and form a lifted flame. In case of the latter, the location would be of prime importance as owing to small dimensions, it may not be desired to have flame anchored beyond a certain percentage of the reactor channel length. Thus, for designing an appropriate reactor channel to achieve these objectives, it is essential to have understanding of the flame propagation dynamics. For quantitative evaluation of the flame speed, we used the definition given by Ruestsch and Broadwell

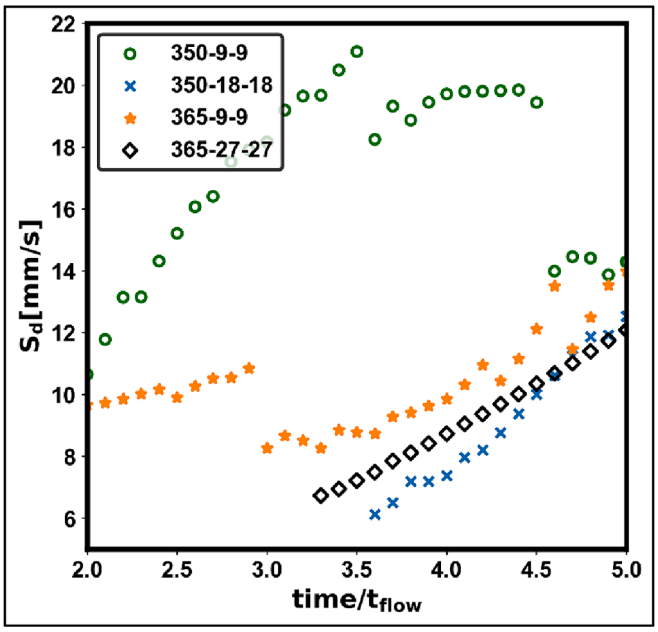

Fig. 18. S_dAs defined in eq. (19) at point of maximum HRR (ignition kernel) for various cases post autoignition phase.

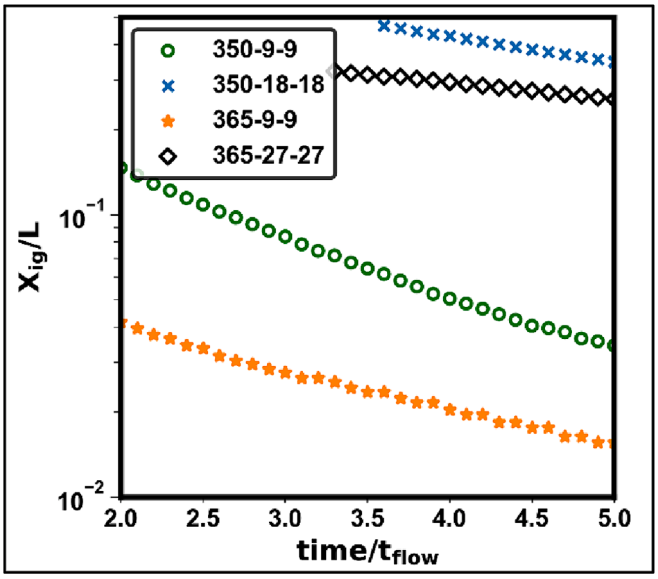

Fig. 19. X-coordinate of HRR_{max}(triple point) for different cases. For better visualization, y-axis has been plotted on the log-scale.

[75] and is given by the following expression,

$$S_d = \frac{1}{\rho|\nabla Y_k|}\left(\nabla \bullet (\rho D \nabla Y_k) + \dot{\omega}_k\right) \tag{19}$$

The relation given by Eq. (19) describes the propagation speed of the *iso*-surface of a progress variable along its normal. This local flame speed is related to the involved chemical dynamics [72,75]. In addition, a propagation speed is also defined which represents how the flame moves as a whole. This can be obtained by accounting for the local fluid flow speed in addition to the local flame speed given by Eq. (19). In the current work, we are primarily interested in the local flame speed S_d. It is evident from Eq. (19) that identification of an appropriate species and point/surface is required to evaluate the local flame speed. In the present case where a single step reaction is considered, the only unique product species is carbon dioxide and thus is chosen to evaluate the flame speed as per Eq. (19). An intuitive choice where to consider this expression is the point of maximum *HRR* which represents the ignition kernel. This is shown for various considered in Fig. 18. Here, we have plotted S_d only for time intervals post autoignition in order to be coherent with the definition of local flame propagation speed. It can be seen that the S_d starts to increase with time and eventually tend to a constant value as observed for the case 350 −9 −9. For other cases, attainment of such constant value will need more computational time but based on the initial trend which is analogous to that of 350 −9 −9, a similar behavior can be ascertained. An important inference that can be deduced is that S_d is considerably higher than respective inlet flow velocity in all the cases and thus implied that the flame is not stabilized and will tend to move upstream towards the inlet and is likely to anchor at the base of the inlet. This is further evident from the $x-$ coordinate plot of HRR_{max} (triple point of the flame) over a period of time and is illustrated for various cases in Fig. 19. It can be seen that as the time evolves, the $x-$ coordinate reduces implying that flame moves towards the inlet. This behavior of the hydrothermal can be sought as advantageous especially at microscale. Nevertheless, this also highlights that for the operating conditions considered, in an event of desiring a stabilized lifted flame (which may be required for reasons such as preventing any upstream conduction near the inlet, pre-autoignition near the inlet etc.) design of reactor with appropriate buff body will be required. These aspects along with other future perspective of this work are presented in the next section.

7. Future perspectives and the road ahead for technological development

The presented results demonstrate the feasibility to develop $\mu SCWO-H$ technology for space applications. The current work can be sought as a stepping stone in this area and brings out several key issues that need to be investigated to realize this technology. In this section, we highlight some of these which would also form the basis of future work. Before proceeding further, it is worth mentioning that the research work though motivated for its application primarily for deep space missions involving humans can nevertheless be used for ground based SCWO process, especially for tapping the advantages of microscale, such as lower reaction time, homogeneous reaction, etc.

In the context of application in hand, the numerical investigations have been undertaken for zero-gravity conditions. This implies the absence of natural convection and thus heat loss from the microreactor which otherwise is quite large as compared to macro/mesoscale owing to a higher surface area to volume ratio. Thus, for truly extending this technology for space missions, such as moon/mars where gravity is not negligible, the effect of heat transfer at microscale needs to be addressed which is bound to have a significant impact on the formation and characteristics of hydrothermal flames. While a more detailed investigation is perspective of future work, here we briefly discuss the probable physical impacts. The heat loss is expected to lower the temperature of the fluid within the reactor and thus increase the ignition delay time. For the investigated flow rates and inlet temperature conditions, the maximum threshold flow rate/velocity for the formation of hydrothermal flame would decrease. Furthermore, even though the ignition kernel may be formed, it may not be able to sustain the flame depending on the heat loss rate. This may require to redefine the presented ignition map. Another important aspect which comes along when considering the presence of gravity is its interaction with the flame, which will however depend on the orientation of microreactor with respect to gravity and flow rates. While in the current presented setup (Fig. 1 and Fig. 2), the effect may not be pronounced, but aligning the flow direction vertically would certainly have an influence. As mentioned earlier, the presence of natural convection would lead to the reduction in threshold flow rate at which ignition can occur thereby implying a lower inertial force. Consequently, the effect of gravity will not be negligible and whether

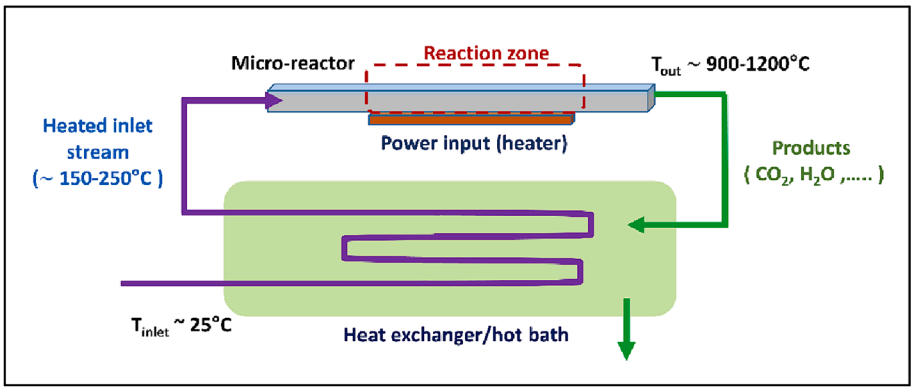

Fig. 20. Schematic illustration of compact *μSCWO* device for operating with minimum energy input.

the flame is momentum or gravity driven needs to be determined and can be characterized using Froude Number. These fundamental questions pave the path for future research work in this direction.

Another important point in any SCWO process has been the energy requirements, mainly related to raising the temperature of the inlet streams to the required value for successful formation of hydrothermal flames in a reactor, which helps to define if the proposed setup is energetically favorable. The microscale size of the reactor in the current setup permits to inject the fluid at ambient conditions and increase the temperature of both the streams only by heating the reactor chip. Owing to small volumes involved, a relatively small amount of heat required as compared to meso/macro scale system can be expected. While a complete energy analysis would require a set of well-established parameters at which the *μSCWO* −*H* is operational, the current work being mainly targeted towards initial demonstration of the process is limited with the required information. However, in order to lay the foundation of further such work, we present a schematic of the final proposed setup (Fig. 20) illustrating how the proposed setup would be energy efficient. The operation of this final technology can be explained as follows. In order to start the reactor, the fluid streams would enter the microreactor at ambient conditions and be heated to desired conditions using the heater – a process similar to one presented in the current work. The products which would be at a higher temperature (900 °C – 1200 °C) would be passed into a hot bath which will acts as a heat exchanger letting the inlet stream to absorb the heat. Thus, over a period of time, the temperature of the inlet stream at the entrance of microreactor would increase. This will depend on the efficiency of the heat exchange and we expect to attain nearly half the required temperature increase through this process. Consequently, the power input to the reactor chip will decrease which would be the only power/energy required to sustain the process. It can thus be seen that a higher temperature at the exit of heat exchanger defines the bottleneck for making this process very close to self-sustaining, a possibility arising thanks to undertaking this process at microscale. This needs to be undertaken in future work for technological realization.

In addition, further research aspects can be ascribed to the design of microreactors, which can lead to formation of hydrothermal flame at high flow velocity. The need for using higher velocity arises from improving the mixing of fuel and oxidizer, which in the presented cases has been largely driven by molecular diffusion. This may require designing reactor channel with appropriate bluff bodies which could serve several purposes, such as creation of local vortices and mixing region to enhance the residence time of the reacting element in the reactor channel and anchoring flames away from the inlet. Another important aspect is the concentration of the fuel required to auto ignite. It is desirable to have the formation of hydrothermal flame with minimal fuel concentration and thus how does varying the fuel and oxidizer ratio governs the evolution of the hydrothermal flame needs to be addressed. An appropriate ignition map needs to be drawn, which could serve as reference for conducting experiments at appropriate conditions.

8. Conclusion

We have presented the first of its kind work experimentally demonstrating the feasibility to realize a microreactor for SCWO oxidation process at 250 bar pressure and temperature 400 °C. The presence of SCWO/hydrothermal flames was captured using optical microscopy. It was found that this observation was not prevalent for all the flow rates. Numerical modelling on a simplified 2D domain was undertaken to understand the physics leading to the formation of hydrothermal flames at microscale and thus distinguish it from a simple SCWO reaction. This was analyzed for two different inlet temperatures below the critical temperature of water for a fixed fuel (ethanol) and oxidizer (oxygen) concentration using a single step reaction chemistry. It was observed that no ignition kernel was formed at high inlet flow velocities ($>$ 40 mm/s). However, at lower flow velocities, because of heat focusing arising due to jet hydrodynamics, increase in the local temperature eventually led to the attainment of autoignition and thus formation of hydrothermal flame. A further analysis of characteristics of hydrothermal flame revealed they exhibit a classical triple flame structure while the local flame speed was significantly higher than the incoming fluid speed resulting in upstream propagation of the triple flame.

CRediT authorship contribution statement

Deewakar Sharma: Writing – review & editing, Writing – original draft, Validation, Software, Methodology, Investigation, Conceptualization. **Olivier Nguyen:** Resources, Methodology. **Fabien Palencia:** Resources, Methodology. **Carole Lecoutre:** Writing – review & editing, Supervision, Project administration, Methodology, Investigation, Conceptualization. **Yves Garrabos:** Methodology, Investigation, Funding acquisition, Conceptualization. **Stéphane Glockner:** Writing – review & editing, Software, Methodology, Investigation. **Samuel Marre:** Writing – review & editing, Supervision, Project administration, Methodology, Investigation, Funding acquisition, Conceptualization. **Arnaud Erriguible:** Writing – review & editing, Supervision, Methodology, Investigation, Conceptualization.

Declaration of competing interest

The authors declare that they have no known competing financial interests or personal relationships that could have appeared to influence the work reported in this paper.

Data availability

Data will be made available on request.

Acknowledgement

The authors would like to thank the French Space Agency CNES for supporting the post-doctoral position of Deewakar Sharma and providing financial support through GdR MFA. The authors also acknowledge support from supercomputing facilities of CNES and the MCIA (Mésocentre de Calcul Intensif Aquitaine) of the University of Bordeaux. Lastly, the authors acknowledge the help of Dr. Kameel Antami during the fabrication of sapphire microreactors.

References

[1] M.D. Bermejo, M.J. Cocero, Supercritical water oxidation: a technical review, AIChE J 52 (11) (2006) 3933–3951, https://doi.org/10.1002/aic.10993.
[2] S. Zhang, Z. Zhang, R. Zhao, J. Gu, J. Liu, B. Örmeci, J. Zhang, A review of challenges and recent Progress in supercritical water oxidation of wastewater, Chem. Eng. Commun. 204 (2) (2017) 265–282, https://doi.org/10.1080/00986445.2016.1262359.
[3] S. Nanda, S.N. Reddy, H.N. Hunter, I.S. Butler, J.A. Kozinski, Supercritical water gasification of lactose as a model compound for valorization of dairy industry effluents, Ind. Eng. Chem. Res. 54 (38) (2015) 9296–9306, https://doi.org/10.1021/acs.iecr.5b02603.
[4] S.N. Reddy, S. Nanda, P. Kumar, M.C. Hicks, U.G. Hegde, J.A. Kozinski, Impacts of oxidant characteristics on the ignition of n-propanol-air hydrothermal flames in supercritical water, Combust. Flame 203 (2019) 46–55, https://doi.org/10.1016/j.combustflame.2019.02.004.
[5] H.L. La Roche, ETH Zurich, 1996.
[6] W. Schilling, E.U. Franck, Combustion and diffusion flames at high pressures to 2000 bar, Ber. Bunsen. Phys. Chem 92 (5) (1988) 631–636, https://doi.org/10.1002/bbpc.198800149.
[7] M. Ren, S. Wang, C. Yang, H. Xu, Y. Guo, D. Roekaerts, Supercritical water oxidation of quinoline with moderate preheat temperature and initial concentration, Fuel 236 (2019) 1408–1414, https://doi.org/10.1016/j.fuel.2018.09.091.
[8] P. Cabeza, M.D. Bermejo, C. Jiménez, M.J. Cocero, Experimental study of the supercritical water oxidation of recalcitrant compounds under hydrothermal flames using tubular reactors, Water Res. 45 (8) (2011) 2485–2495, https://doi.org/10.1016/j.watres.2011.01.029.
[9] LiLi Qian, ShuZhong Wang, Y. Li, Review of Supercritical Water Oxidation in Hydrothermal Flames, Advanced Materials Research 908 (2014) 239-242.
[10] B. Wellig, Transpiring wall reactor for supercritical water oxidation, ETH Zurich (2003).
[11] K.S. Lieball, Numerical investigations on a transpiring wall reactor for supercritical water oxidation, ETH Zurich (2003).
[12] B. Wellig, K. Lieball, P. Rudolf von Rohr, Operating characteristics of a transpiring-wall SCWO reactor with a hydrothermal flame as internal heat source, J. Supercrit. Fluids 34 (1) (2005) 35–50, https://doi.org/10.1016/j.supflu.2004.07.003.
[13] C. Hutter, A. Zenklusen, S. Kuhn, P. Rudolf von Rohr, Large eddy simulation of flow through a streamwise-periodic structure, Chem. Eng. Sci. 66 (3) (2011) 519–529, https://doi.org/10.1016/j.ces.2010.11.015.
[14] C. Hutter, A. Zenklusen, R. Lang, P. Rudolf von Rohr, Axial dispersion in heat foams and streamwise-periodic porous media, Chem. Eng. Sci. 66 (6) (2011) 1132–1141, https://doi.org/10.1016/j.ces.2010.12.016.
[15] T. Rothenfluh, M.J. Schuler, P.R. von Rohr, Penetration length studies of supercritical water jets submerged in a subcritical water environment using a novel optical Schlieren method, J. Supercrit. Fluids 57 (2) (2011) 175–182, https://doi.org/10.1016/j.supflu.2011.02.018.
[16] M.D. Bermejo, P. Cabeza, M. Bahr, R. Fernández, V. Ríos, C. Jiménez, M.J. Cocero, Experimental study of hydrothermal flames initiation using different static mixer configurations, J. Supercrit. Fluids 50 (3) (2009) 240–249, https://doi.org/10.1016/j.supflu.2009.06.010.
[17] M.D. Bermejo, P. Cabeza, J.P.S. Queiroz, C. Jiménez, M.J. Cocero, Analysis of the scale up of a transpiring wall reactor with a hydrothermal flame as a heat source for the supercritical water oxidation, J. Supercrit. Fluids 56 (2011) 21–32.
[18] P. Cabeza, J.P.S. Queiroz, S. Arca, C. Jiménez, A. Gutiérrez, M.D. Bermejo, M. J. Cocero, Sludge destruction by means of a hydrothermal flame. optimization of ammonia destruction conditions, Chem. Eng. J. 232 (2013) 1–9, https://doi.org/10.1016/j.cej.2013.07.040.
[19] P. Cabeza, J.P. Silva Queiroz, M. Criado, C. Jiménez, M.D. Bermejo, F. Mato, M. J. Cocero, Supercritical water oxidation for energy production by hydrothermal flame as internal heat source. experimental results and energetic study, Energy 90 (2015) 1584–1594, https://doi.org/10.1016/j.energy.2015.06.118.
[20] C. Narayanan, C. Frouzakis, K. Boulouchos, K. Príkopský, B. Wellig, P. Rudolf von Rohr, Numerical modelling of a supercritical water oxidation reactor containing a hydrothermal flame, J. Supercrit. Fluids 46 (2) (2008) 149–155, https://doi.org/10.1016/j.supflu.2008.04.005.
[21] T. Meier, M.J. Schuler, P. Stathopoulos, B. Kramer, P. Rudolf von Rohr, Hot surface ignition and monitoring of an internal oxygen–ethanol hydrothermal flame at 260bar, J. Supercrit. Fluids 130 (2017) 230–238, https://doi.org/10.1016/j.supflu.2016.09.015.
[22] T. Meier, P. Stathopoulos, P. Rudolf von Rohr, Hot surface ignition of oxygen–ethanol hydrothermal flames, J. Supercrit. Fluids 107 (2016) 462–468, https://doi.org/10.1016/j.supflu.2014.11.012.
[23] P. Stathopoulos, Hydrothermal spallation drilling experiments in a novel high ppressure pilot plant, ETH Zurich, Switzerland, 2013.
[24] A. Sobhy, I.S. Butler, J.A. Kozinski, Selected profiles of high-pressure methanol–air flames in supercritical water, Proc. Combust. Inst. 31 (2) (2007) 3369–3376, https://doi.org/10.1016/j.proci.2006.07.253.
[25] A. Sobhy, R.I.L. Guthrie, I.S. Butler, J.A. Kozinski, Naphthalene combustion in supercritical water flames, Proc. Combust. Inst. 32 (2) (2009) 3231–3238, https://doi.org/10.1016/j.proci.2008.06.173.
[26] R.M. Serikawa, T. Usui, T. Nishimura, H. Sato, S. Hamada, H. Sekino, Hydrothermal flames in supercritical water oxidation: investigation in a pilot scale continuous reactor, Fuel 81 (9) (2002) 1147–1159, https://doi.org/10.1016/S0016-2361(02)00015-7.
[27] M. Ren, S. Wang, J. Zhang, Y. Guo, D. Xu, Y. Wang, Characteristics of methanol hydrothermal combustion: detailed chemical kinetics coupled with simple flow modeling study, Ind. Eng. Chem. Res. 56 (18) (2017) 5469–5478, https://doi.org/10.1021/acs.iecr.7b00886.
[28] M. Ren, S. Wang, N. Romero-Anton, J. Zhao, C. Zou, D. Roekaerts, Numerical study of a turbulent co-axial non-premixed flame for methanol hydrothermal combustion: comparison of the EDC and FGM models, J. Supercrit. Fluids 169 (2021) 105132, https://doi.org/10.1016/j.supflu.2020.105132.
[29] C. Cui, Y. Li, S. Wang, M. Ren, C. Yang, Z. Jiang, J. Zhang, Review on an Advanced Combustion Technology: Supercritical Hydrothermal Combustion, Applied Sciences 10(5) (2020). https://doi.org/10.3390/app10051645.
[30] C. Song, K. Luo, T. Jin, H. Wang, J. Fan, Direct numerical simulation on auto-ignition characteristics of turbulent supercritical hydrothermal flames, Combust. Flame 200 (2019) 354–364, https://doi.org/10.1016/j.combustflame.2018.12.002.
[31] C. Song, T. Jin, H. Wang, Z. Gao, K. Luo, J. Fan, High-fidelity numerical analysis of non-premixed hydrothermal flames: flame structure and stabilization mechanism, Fuel 259 (2020) 116162, https://doi.org/10.1016/j.fuel.2019.116162.
[32] T. Jin, C. Song, H. Wang, Z. Gao, K. Luo, J. Fan, Direct numerical simulation of a supercritical hydrothermal flame in a turbulent jet, J. Fluid Mech. 922 (2021) A8, https://doi.org/10.1017/jfm.2021.535.
[33] M.C. Hicks, U.G. Hegde, J.W. Fisher, Investigation of supercritical water phenomena for space and extraterrestrial application, NASA (2012).
[34] M.C. Hicks, U.G. Hegde, J.J. Kojima, Hydrothermal ethanol flames in co-flow jets, J. Supercrit. Fluids 145 (2019) 192–200, https://doi.org/10.1016/j.supflu.2018.12.010.
[35] S. Deewakar, E. Arnaud, N. Oliver, L. Carole, G. Yves, H. Uday, H. Mike, M. Samuel, A preliminary investigation of microreactor designs for supercritical water oxidation using hydrothermal flames for space applications, International Symposium on Supercritical Fluids, Montreal, Canada, 2022.
[36] S. Marre, C. Lecoutre, Y. Garrabos, C. Fauveau, A. Cario, O. Nguyen, Centre National dEtudes Spatiales CNES and Centre National de la Recherche Scientifique CNRS, 2023. Sapphire microreactors.
[37] D. Sharma, C. Lecoutre, F. Palencia, O. Nguyen, A. Erriguible, S. Marre, Assessment of machine learning algorithms for predicting autoignition and ignition delay time in microscale supercritical water oxidation process, Fuel 352 (2023) 129098, https://doi.org/10.1016/j.fuel.2023.129098.
[38] S. Marre, A. Adamo, S. Basak, C. Aymonier, K.F. Jensen, Design and packaging of microreactors for high pressure and high temperature applications, Ind. Eng. Chem. Res. 49 (22) (2010) 11310–11320, https://doi.org/10.1021/ie101346u.
[39] D. Sharma, Arnaud Erriguible, Gurunath Gandikota, Daniel Beysens, S. Amiroudine, Vibration-induced thermal instabilities in supercritical fluids in the absence of gravity, Physical Review F (2018, Under Revision).
[40] D. Sharma, A. Erriguible, S. Amiroudine, Cooling beyond the boundary value in supercritical fluids under vibration, Phys. Rev. E 96 (6) (2017) 063102.
[41] S. Amiroudine, J.P. Caltagirone, A. Erriguible, A lagrangian-eulerian compressible model for the trans-critical path of near-critical fluids, Int. J. Multiph. Flow 59 (2014) 15–23, https://doi.org/10.1016/j.ijmultiphaseflow.2013.10.008.
[42] K. Koido, K. Hirosaka, T. Kubo, M. Fukayama, K. Ouryouji, T. Hasegawa, Numerical study on premixed hydrothermal combustion in tube reactor, Combust. Theor. Model. 13 (2) (2009) 295–318, https://doi.org/10.1080/13647830802617698.
[43] Bonnie J. McBride, Sanford Gordon, M.A. Reno, Coefficients for Calculating Thermodynamic and Transport Properties of Individual Species, NASA Technical Memorandum 1993.
[44] Z. Gao, H. Wang, C. Song, K. Luo, J. Fan, Real-fluid effects on laminar diffusion and premixed hydrothermal flames, J. Supercrit. Fluids 153 (2019) 104566, https://doi.org/10.1016/j.supflu.2019.104566.
[45] D. Sharma, A. Erriguible, G. Gandikota, D. Beysens, S. Amiroudine, Vibration-induced thermal instabilities in supercritical fluids in the absence of gravity, Phys. Rev. Fluids 4 (3) (2019) 033401, https://doi.org/10.1103/PhysRevFluids.4.033401.
[46] T.H. Chung, M. Ajlan, L.L. Lee, K.E. Starling, Generalized multiparameter correlation for nonpolar and polar fluid transport properties, Ind. Eng. Chem. Res. 27 (4) (1988) 671–679, https://doi.org/10.1021/ie00076a024.
[47] Nist, Thermophysical properties of pure fluids database, NIST12, NIST, Gaithersburg MD, 2000.
[48] R.C. Reid;, J.M. Prausnitz;, B.E. Poling, The Properties of Gases and Liquids, 4th ed., McGraw-Hill1987.
[49] E. Masi, J. Bellan, K.G. Harstad, N.A. Okong'o, Multi-species turbulent mixing under supercritical-pressure conditions: modelling, direct numerical simulation

and analysis revealing species spinodal decomposition, Journal of Fluid Mechanics 721 (2013) 578–626, https://doi.org/10.1017/jfm.2013.70.
[50] S. Glockner, A.M.D. Jost, A. Erriguible, Advanced petascale simulations of the scaling up of mixing limited flow processes for materials synthesis, Chem. Eng. J. 431 (2022) 133647, https://doi.org/10.1016/j.cej.2021.133647.
[51] A.M.D. Jost, S. Glockner, A. Erriguible, Direct numerical simulations of fluids mixing above mixture critical point, J. Supercrit. Fluids 165 (2020) 104939, https://doi.org/10.1016/j.supflu.2020.104939.
[52] C. Hirsch, Numerical Computation of Internal and External Flows: Computational Methods for Inviscid and Viscous Flows, Wiley-Blackwell1990.
[53] T.J. Poinsot, S.K. Lelef, Boundary conditions for direct simulations of compressible viscous flows, J. Comput. Phys. 101 (1) (1992) 104–129, https://doi.org/10.1016/0021-9991(92)90046-2.
[54] A. Mani, Analysis and optimization of numerical sponge layers as a nonreflective boundary treatment, J. Comput. Phys. 231 (2) (2012) 704–716, https://doi.org/10.1016/j.jcp.2011.10.017.
[55] J. Doom, Y. Hou, K. Mahesh, A numerical method for DNS/LES of turbulent reacting flows, J. Comput. Phys. 226 (1) (2007) 1136–1151, https://doi.org/10.1016/j.jcp.2007.05.037.
[56] D.J. Bodony, Analysis of sponge zones for computational fluid mechanics, J. Comput. Phys. 212 (2) (2006) 681–702, https://doi.org/10.1016/j.jcp.2005.07.014.
[57] D. Sharma, A. Erriguible, S. Amiroudine, Numerical modeling of the impact pressure in a compressible liquid medium: application to the slap phase of the locomotion of a basilisk lizard, Theor. Comput. Fluid Dyn. 31 (2017) 281–293, https://doi.org/10.1007/s00162-017-0422-4.
[58] Y. Feng, M. Tayyab, P. Boivin, A lattice-boltzmann model for low-mach reactive flows, Combust. Flame 196 (2018) 249–254, https://doi.org/10.1016/j.combustflame.2018.06.027.
[59] I. Dhuchakallaya, A.P. Watkins, Auto-ignition of diesel spray using the PDF-Eddy break-up model, App. Math. Model. 34 (7) (2010) 1732–1745, https://doi.org/10.1016/j.apm.2009.09.019.
[60] S.H. Kang, S.W. Baek, J.H. Choi, Autoignition of sprays in a cylindrical combustor, Int. J. Heat Mass Transf. 44 (13) (2001) 2413–2422, https://doi.org/10.1016/S0017-9310(00)00283-0.
[61] T. Rente, V.I. Golovitchev, I. Denbratt, 1–08) numerical study of n-heptane spray auto-ignition at different levels of pre-ignition TURBULENCE((DE-3)Diesel engine combustion 3-modeling, The Proceedings of the International Symposium on Diagnostics and Modeling of Combustion in Internal Combustion Engines 01 (204) (2001) 12, https://doi.org/10.1299/jmsesdm.01.204.12.
[62] J.B. Heywood, Internal combustion engine fundamental, McGraw-Hill International, New York, 1988.
[63] C.K. Law, Combustion Physics, Cambridge University Press, Cambridge, 2006. https://doi.org/DOI: 10.1017/CBO9780511754517.
[64] E. Mastorakos, T.A. Baritaud, T.J. Poinsot, Numerical simulations of autoignition in turbulent mixing flows, Combust. Flame 109 (1) (1997) 198–223, https://doi.org/10.1016/S0010-2180(96)00149-6.
[65] J.J. Kojima, U.G. Hegde, D.J. Gotti, M.C. Hicks, Flame structure of supercritical ethanol/water combustion in a co-flow air stream characterized by raman chemical analysis, J. Supercrit. Fluids 166 (2020) 104995, https://doi.org/10.1016/j.supflu.2020.104995.
[66] K.K.-y. Kuo, Principles of Combustion, John Wiley & Sons, Inc, New Jersey, 2005.
[67] C.K. Law, S. Ishizuka, P. Cho, On the opening of premixed bunsen flame tips, Combust. Sci. Technol. 28 (3–4) (1982) 89–96, https://doi.org/10.1080/00102208208952545.
[68] P. Domingo, L. Vervisch, Triple flames and partially premixed combustion in autoignition of non-premixed turbulent mixtures, Symposium (international) on Combustion 26(1) (1996) 233–240, https://doi.org/10.1016/S0082-0784(96)80221-9.
[69] H.G. Im, J.H. Chen, C.K. Law, Ignition of hydrogen-air mixing layer in turbulent flows, Symposium (international) on Combustion 27(1) (1998) 1047–1056, https://doi.org/10.1016/S0082-0784(98)80505-5.
[70] T. Yao, W.H. Yang, K.H. Luo, Direct numerical simulation study of hydrogen/air auto-ignition in turbulent mixing layer at elevated pressures, Comput. Fluids 173 (2018) 59–72, https://doi.org/10.1016/j.compfluid.2018.03.075.
[71] T. Echekki, J.H. Chen, Structure and propagation of methanol-air triple flames, Combust. Flame 114 (1) (1998) 231–245, https://doi.org/10.1016/S0010-2180(97)00287-3.
[72] G.R. Ruetsch, L. Vervisch, A. Liñán, Effects of heat release on triple flames, Phys. Fluids 7 (6) (1995) 1447–1454, https://doi.org/10.1063/1.868531.
[73] H. Yamashita, M. Shimada, T. Takeno, A numerical study on flame stability at the transition point of jet diffusion flames, Symposium (international) on Combustion 26(1) (1996) 27–34, https://doi.org/10.1016/S0082-0784(96)80196-2.
[74] C.S. Yoo, R. Sankaran, J.H. Chen, Three-dimensional direct numerical simulation of a turbulent lifted hydrogen jet flame in heated coflow: flame stabilization and structure, J. Fluid Mech. 640 (2009) 453–481, https://doi.org/10.1017/S0022112009991388.
[75] G. Ruetsch, J. Broadwell, Effects of confinement on partially premixed flames, Annual Research Briefs 1995 (1995).